journal

J. Am. Ceram. Soc., **88** [11] 2979–2997 (2005)
DOI: 10.1111/j.1551-2916.2005.00740.x

Impedance Spectroscopy as a Tool for Chemical and Electrochemical Analysis of Mixed Conductors: A Case Study of Ceria

Wei Lai and Sossina M. Haile[†]

Materials Science, California Institute of Technology, Pasadena, California 91125

The AC impedance response of mixed ionic and electronic conductors (MIECs) is derived from first principles and quantitatively compared with experimental data. While the approach is not entirely new, the derivation is provided in a unified and comprehensive manner. Using $Sm_{0.15}Ce_{0.85}O_{1.925-\delta}$ with Pt electrodes as a model system, a broad spectrum of electrical and thermodynamic properties is extracted solely from the measurement of impedance spectra over wide oxygen partial pressure and temperature ranges. Here, the oxygen partial pressure was varied from air [$p_{O_2} = 0.21$ atm] to H_2 [$p_{O_2} = 10^{-31}$ atm], and the temperature was varied from 500° to 650°C. It was essential for this analysis that the material under investigation exhibit, under some conditions, purely ionic behavior and, under others, mixed conducting behavior. The transition from ionic to mixed conducting behavior is recognizable not only from the oxygen partial pressure dependence of the total conductivity but also directly from the shape of the impedance spectra. Within the electrolytic regime, the impedance spectra (presented in Nyquist form) take the shape of simple, depressed arcs, whereas within the mixed conducting regime (under reducing conditions), the spectra exhibit the features associated with a half tear-drop-shaped element. Parameters derived from quantitative fitting of the impedance spectra include the concentration of free electron carriers, the mobilities and activation energies for both ion and electron transport, the electrolytic domain boundary, and the entropy and enthalpy of reduction. In addition, the electrochemical behavior of O_2 and H_2 at the Pt|ceria interface has been characterized from these measurements. Under oxidizing conditions, the data suggest an oxygen electrochemical reaction that is rate limited by the dissociated adsorption/diffusion of oxygen species on the Pt electrode, similar to Pt|YSZ (yttria-stabilized zirconia). Under reducing conditions, the inverse of the electrode resistivity obeys a $p_{O_2}^{-1/4}$ dependence, with an activation energy that is similar to that measured for the electronic conductivity. These results suggest that ceria is electrochemically active for hydrogen electro-oxidation and that the reaction is limited by the rate of removal of electrons from the ceria surface.

D. Johnson—contributing editor

Manuscript No. 20634. Received June 2, 2005; approved August 23, 2005.
Funding for this work has been provided by ONR, Office of Electrochemical Power Science and Technology through the MURI program.
[†]Author to whom correspondence should be addressed. e-mail: smhaile@caltech.edu

I. Introduction

AC impedance spectroscopy is a valuable tool for studying both the bulk transport properties of a material and the electrochemical reactions on its surface.[1,2]. Well over 7000 papers using this technique appear in the Institute for Scientific Information (ISI) database for the 20-years time period from 1985 to date, Fig. 1.[3] Of these, approximately two-thirds are devoted to bulk and electrode processes, approximately one-quarter to corrosion, and the remainder to other topics such as coatings and bio-electrical processes. For comparison, it is noteworthy that in this same time period, which covers the height of activity in superconductor research, approximately 6000 papers using the Hall effect appear. The value of AC impedance spectroscopy derives from the effectiveness of the technique in isolating individual reaction/migration steps in a multistep process. That is, because each reaction or migration step has, ideally, a unique time constant associated with it, these steps can be separated in the frequency domain. Experimentally, one applies a small sinusoidal current perturbation to an equilibrium system and measures the corresponding voltage response. The ratio of the voltage response to the current perturbation is the impedance.

Typically, AC impedance experiments are carried out over a wide range of frequencies (several millihertz to several megahertz), and the interpretation of the resulting spectra is aided by analogy to equivalent circuits involving simple components such as resistors and capacitors. In general, such equivalent circuits are not unique, and indeed there exists an infinite set of circuits that can represent any given impedance. It is common to select a physically plausible circuit containing a minimal number of components and, in a somewhat *ad hoc* manner, assign physical significance to the derived parameters. Often, a meaningful insight into material behavior can be gained from such analyses, which certainly explains the rise in popularity of impedance spectroscopy as a materials characterization tool, Fig. 1. However, the *ad hoc* approach is lacking in mathematical and physical rigor, and can lead one to overlook some of the more subtle, but significant, features of the data.

A key characteristic of the impedance spectra collected from mixed ionic and electronic conductors (MIECs), where the MIEC is placed between two metal electrodes, is the presence of a half tear-drop-shaped feature in the Nyquist ($-Z_{imag}$ versus Z_{real}) representation. The earliest treatment of a related problem is the classic work of Warburg, who studied diffusion under AC conditions in an electrolyte placed between two identical

Feature

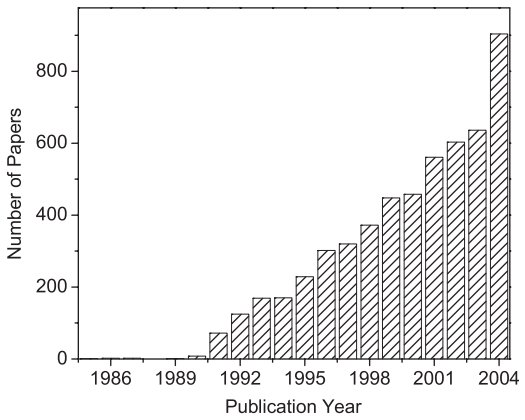

Fig. 1. Number of papers published annually with the words "impedance spectroscopy" in the title, abstract, or key words list.

electrodes.[4,5] The essence of Warburg's analysis is to solve Fick's laws of diffusion under the appropriate boundary conditions.

Since that early work, two parallel schools of thought have appeared in the literature for rationalizing the the half teardrop-shaped arc obtained from MIECs, both of which can be viewed as outgrowths of Warburg's original analysis. The first, as proposed by Boukamp,[6,7] is to account explicitly for the possibility that there are sources and/or sinks in the material such that the overall rate of charge flux is co-limited by both chemical and electrochemical reactions. Introduction of a source/sink term into the mathematical formalism results in the so-called Gerischer impedance element. An analogous approach has been applied by Adler[8] for the case where the flux is co-limited by a combined chemical–electrochemical reaction sequence at the electrode rather than within the bulk of the material. Here, the electrolyte need not be a mixed conductor, and indeed the analysis has been applied to the pure ionic conductor yttria-stabilized zirconia (YSZ). Furthermore, the electrode may be a simple metal, such as Pt, or a mixed conductor itself, such as $(La,Sr)CoO_{3-\delta}$ (LSC). This approach has its roots in earlier work by Sluyters-Rehbach and Sluyters,[9] Robertson and Michaels,[10] and the original work of Gerischer.[11] Modeling impedance spectra in this manner (i.e., using the Gerischer element) requires that some sort of chemical step, which may or may not be known *a priori*, be invoked. For the case in which this step is presumed to occur at the electrode, adsorption and diffusion are obvious candidates. In contrast, if this step is presumed to occur within the mixed conducting electrolyte, it is not at all apparent what the reaction might be. As one alternative, Boukamp has suggested that the reaction might involve the formation of immobile complexes within the bulk of the MIEC.[7]

A second school of thought for understanding the half teardrop-shaped arc in the impedance spectrum of MIECs follows from recent works of Jamnik and Maier[12,13] and of Horno *et al.*,[14] and has its roots in earlier studies by Macdonald[15] and by Brumleve and Buck.[16] These authors explicitly account for the fact that the diffusing charged species is exposed to an electrical as well as a chemical potential gradient. The flux equations can then be mapped to an equivalent circuit, providing a first principles representation of an MIEC. For a variety of reasons outlined below, this model, in which the influence of the internal electric field gradient is treated in full, rather than the chemical–electrochemical reaction model, is taken to represent MIEC behavior, accurately as observed here.

In the present study, an alternate (and, we believe, more physically intuitive) derivation of the equivalent circuit proposed by Jamnik and Maier[13] is provided, and the analysis is then applied to the evaluation of ceria. It is shown that not only can one extract the important electrical parameters of an MIEC as indicated by the earlier work but also, from measurements carried out over wide oxygen partial pressures and at a range of temperatures, essential thermodynamic parameters. The measurements and analysis, furthermore, provide some indication as to the rate-limiting step for hydrogen electro-oxidation at the metal|ceria interface. A preliminary attempt to carry out a similar analysis (limited, however, to the behavior of ceria and not addressing the Pt|ceria interface) has recently been reported by Atkinson *et al.*,[17] and a comparison with the results of these authors is also presented here.

Ceria has been selected for study because of increasing interest in this material as an electrolyte for "reduced"-temperature solid oxide fuel cells (SOFCs),[18] that is, SOFCs in which the traditional operating temperature of 800°–1000°C has been reduced to 500°–800°C. Samaria-doped ceria (SDC) and gadolinia-doped ceria (GDC) exhibit higher conductivity than YSZ at 700°C, and it has been possible to obtain power densities as high as 1 W/cm^2 from anode-supported SDC fuel cells at 600°C using humidified hydrogen as the fuel and air as the oxidant.[19] Fuel cell operation in this intermediate-temperature regime has the potential for substantially lowering auxiliary component costs and increasing the thermomechanical stability of the SOFC system. The large body of experimental data already existent for acceptor-doped ceria[20] as a consequence of its value for fuel cell applications renders this an ideal model material against which to verify a new measurement approach, whereas the new insight that is to be gained from careful analysis of impedance data into electrocatalytic pathways is of great value to the design of SOFC electrodes.

II. Theoretical Background

(1) AC Impedance of a Mixed Ionic and Electronic Conductor

(A) Fundamental Physics: Mass and charge transport in solids subjected to a combined electrical and chemical potential gradient is governed by the so-called diffusion–drift equation (or Nernst–Planck equation), the derivation of which is given in many texts (cf. Richert[21]). For the one-dimensional case, this equation has the form

$$J_i^{\text{mass}}(x,t) = -D_i \frac{\partial c_i(x,t)}{\partial x} - \frac{\sigma_i(x,t)}{z_i e} \frac{\partial \phi(x,t)}{\partial x} \tag{1}$$

where x is the position, t is the time, J_i^{mass} is the mass flux of the charged species i, D_i is the diffusion coefficient, c_i is the concentration, σ_i is the conductivity, $z_i e$ is the charge carried by the species, e is the charge of an electron, and ϕ is the electrical potential. In general c_i, σ_i, and ϕ can each vary with both time and position. The first term in the diffusion–drift equation reflects a statement of Fick's law, whereas the second reflects a statement of Ohm's law, modified to translate charge flux (or current density), J_i^{charge}, to mass flux according to $J_i^{\text{charge}} = z_i e J_i^{\text{mass}}$.

For an ideal solution, in which there is a simple relationship between the concentration and chemical potential, μ, the diffusion–drift equation can be readily rewritten in terms of the gradient in a single quantity, the electrochemical potential, $\tilde{\mu}$. Specifically, the chemical potential of an ideal solution is given as

$$\mu_i(x,t) = \mu_i^0 + k_B T \ln\, c_i(x,t) \tag{2}$$

where $\mu_i^0$is the standard chemical potential, k_B is the Boltzmann constant, and T is the absolute temperature. Differentiating with respect to x yields

$$\frac{\partial \mu_i(x,t)}{\partial x} = \frac{k_B T}{c_i(x,t)} \frac{\partial c_i(x,t)}{\partial x} \tag{3}$$

and substituting Eq. (3) into Eq. (1) yields

$$J_i^{\text{mass}}(x,t) = -\frac{D_i c_i(x,t)}{k_B T} \frac{\partial \mu_i(x,t)}{\partial x} - \frac{\sigma_i(x,t)}{z_i e} \frac{\partial \phi(x,t)}{\partial x} \tag{4}$$

Now making use of the Nernst–Einstein relationship relating conductivity to diffusivity

$$\sigma_i(x,t) = \frac{(z_i e)^2 c_i(x,t)}{k_B T} D_i \tag{5}$$

and combining the chemical and electrical contributions to the potential via the electrochemical potential

$$\tilde{\mu}_i(x,t) = \mu_i(x,t) + z_i e \phi(x,t) \tag{6}$$

one obtains

$$J_i^{\text{mass}}(x,t) = -\frac{\sigma_i(x,t)}{(z_i e)^2} \frac{\partial \tilde{\mu}_i(x,t)}{\partial x} \tag{7}$$

This form of the diffusion–drift equation is the first of three fundamental equations of relevance to the treatment here of fluxes of charged species through a mixed conductor.

In the case where the concentration of species i changes with time and there are no sources or sinks of mass, the variation in mass flux with position must balance the variation in concentration with time according to the continuity equation

$$\frac{\partial J_i^{\text{mass}}(x,t)}{\partial x} + \frac{\partial c_i(x,t)}{\partial t} = 0 \tag{8}$$

This relationship provides a second constraint in the description of mass flow in the system. For an ideal solution (the chemical potential of which is described by Eq. (2)), the temporal derivative of concentration is obtained from

$$\frac{\partial \mu_i(x,t)}{\partial t} = \frac{k_B T}{c_i(x,t)} \frac{\partial c_i(x,t)}{\partial t} \tag{9}$$

and, thus, the continuity equation implies

$$\frac{\partial J_i^{\text{mass}}(x,t)}{\partial x} = -\frac{c_i(x,t)}{k_B T} \frac{\partial \mu_i(x,t)}{\partial t} \tag{10}$$

This is the second fundamental equation describing the flux of charged species through a mixed conductor.

One must next consider the effect of a time-varying electrical field (as is experimentally applied) on the flow of charge in the system. Charge flux must, like mass flux, obey the laws of continuity. In order to rewrite Eq. (8) appropriately, one makes use of the previously noted relationship between charge and mass flux

$$J_i^{\text{charge}}(x,t) = z_i e J_i^{\text{mass}}(x,t) \tag{11}$$

to obtain

$$\frac{\partial}{\partial x} J_i^{\text{charge}}(x,t) + \frac{\partial}{\partial t}[e z_i c_i(x,t)] = 0 \tag{12}$$

As Eq. (12) is true for any particular species, it must also be true for the sum of all the species such that

$$\frac{\partial}{\partial x} \sum_i J_i^{\text{charge}}(x,t) + \frac{\partial}{\partial t}\left[\sum_i e z_i c_i(x,t)\right] = 0 \tag{13}$$

The sum of all the charges in the system, $\sum_i e z_i c_i(x,t)$, is related to the electrical potential via Poisson's equations

$$-\varepsilon_r(x,t)\varepsilon_0 \frac{\partial^2 \phi(x,t)}{\partial x^2} = \sum_i e z_i c_i(x,t) \tag{14}$$

where ε_r is the relative permittivity of the material under consideration and ε_0 is the permittivity of vacuum. Insertion into Eq. (13) yields

$$\frac{\partial}{\partial x} \sum_i J_i^{\text{charge}}(x,t) + \frac{\partial}{\partial x}\left\{-\frac{\partial}{\partial t}\left[\varepsilon_r(x,t)\varepsilon_0 \frac{\partial \phi(x,t)}{\partial x}\right]\right\} = 0 \tag{15}$$

which implies that the total charge flux is

$$J_T^{\text{charge}}(t) = \sum_i J_i^{\text{charge}}(x,t) + J_{\text{dis}}^{\text{charge}}(x,t) \tag{16}$$

where

$$J_{\text{dis}}^{\text{charge}}(x,t) = -\frac{\partial}{\partial t}\left[\varepsilon_r(x,t)\varepsilon_0 \frac{\partial \phi(x,t)}{\partial x}\right] \tag{17}$$

Thus, the time-varying electrical field produces what is termed a displacement flux, $J_{\text{dis}}^{\text{charge}}$, and its behavior yields the third fundamental equation describing the flux of charged species through a mixed conductor.

Rewriting Eqs. (7) and (10) in terms of charge rather than mass flux enables one to unify the three independent constraints on the flow of charged species. This is achieved by making use of Eq. (11) and by also defining two new types of potentials. The first is the electrical equivalent of the chemical potential,

$$\mu_i^*(x,t) = \frac{\mu_i(x,t)}{z_i e} \tag{18}$$

and the second the electrical equivalent of the electrochemical potential,

$$\tilde{\mu}_i^*(x,t) = \mu_i^*(x,t) + \phi(x,t) \tag{19}$$

both of which have units of electrical potential. Inserting Eqs. (11), (18), and (19) into Eqs. (7) and (10), respectively, yields

$$J_i^{\text{charge}}(x,t) = -\sigma_i(x,t) \frac{\partial \tilde{\mu}_i^*(x,t)}{\partial x} \tag{20}$$

and

$$\frac{\partial}{\partial x} J_i^{\text{charge}}(x,t) = -\frac{(z_i e)^2 c_i(x,t)}{k_B T} \frac{\partial \mu_i^*(x,t)}{\partial t} \tag{21}$$

which, along with Eq. (17), entirely describes the current flow in the material system. From the additive nature of the fluxes, Eq. (16), it is apparent that the processes must exist in parallel with one another.

If the system is exposed to a uniform chemical potential environment over the course of the impedance measurement, the position dependence of the material properties (σ_i, c_i and ε_r) can be ignored. Furthermore, if the voltage perturbations are small, the time-dependent material properties can be replaced with their time-averaged values, and these averages are implied hereafter. Thus, for small perturbations $\Delta\phi$ and $\Delta\tilde{\mu}_i$, the fluxes $\Delta J_i^{\text{charge}}$ and $\Delta J_{\text{dis}}^{\text{charge}}$ obey the following equations:

$$\Delta J_i^{\text{charge}}(x,t) = -\sigma_i \frac{\partial}{\partial x} \Delta\tilde{\mu}_i^*(x,t) \tag{22}$$

$$\frac{\partial}{\partial x} \Delta J_i^{\text{charge}}(x,t) = -\frac{(z_i e)^2 c_i}{k_B T} \frac{\partial}{\partial t} \Delta\mu_i^*(x,t) \tag{23}$$

$$\Delta J_{\text{dis}}^{\text{charge}}(x,t) = -\varepsilon_r \varepsilon_0 \frac{\partial}{\partial x} \frac{\partial}{\partial t} \Delta\phi(x,t) \tag{24}$$

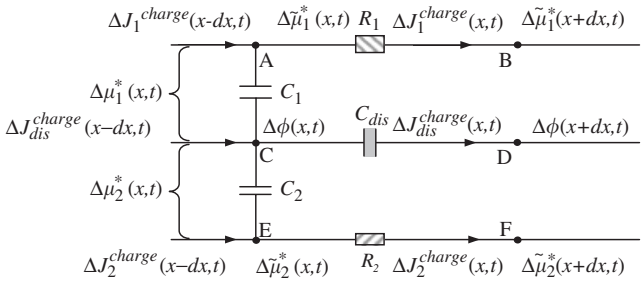

Fig. 2. Differential element of the equivalent circuit obeying the current flow constraints Eqs. (22)–(24) for a system in which two charge-carrying species are mobile. The current associated with species 1 flows along the top rail, whereas that associated with species 2 flows along the bottom rail. The central rail supports current flow because of capacitive effects. In principle, flow between rails is possible. The electrical potential at each of the branchpoints is indicated as is the entering flux. The resistors and capacitors in the system can have position-dependent values, but otherwise behave as standard resistor and capacitor elements. A is the cross-sectional area of the element and dx is its length.

(B) Equivalent Circuit Representation: As noted by Jamnik and Maier[12] and demonstrated earlier by Brumleve and Buck,[16] the system of coupled differential equations given above can be mapped onto an equivalent circuit whose components correspond to physically significant quantities. For the case where there are two mobile charge-carrying species (dopants in this system are taken to be immobile), a differential (dx) portion of the circuit that represents Eqs. (22)–(24) is as shown in Fig. 2. The element has a cross-sectional area A. Species 1 flows along rail 1 ($\overline{AB}$) and species 2 flows along rail 2 ($\overline{EF}$). The displacement current density flows along the central, displacement rail ($\overline{CD}$), and additional flow between rails is, in principle, possible. The electrical potentials at branchpoints A, C, and E are given by $\Delta\tilde{\mu}_1^*(x,t)$, $\Delta\phi(x,t)$ and $\Delta\tilde{\mu}_2^*(x,t)$, respectively, whereas at x+dx, branchpoints B, D, and F, have analogous electrical potentials of $\Delta\tilde{\mu}_1^*(x+\mathrm{d}x,t)$, $\Delta\phi(x+\mathrm{d}x,t)$, and $\Delta\tilde{\mu}_2^*(x+\mathrm{d}x,t)$, respectively. From Eq. (19), it is apparent that the "voltage" difference between branchpoints A and C is $\Delta\mu_1^*(x,t)$ and that between E and C is $\Delta\mu_2^*(x,t)$. In fact, there is no electric potential drop between these branchpoints and this "voltage" is a mathematical consequence of having renormalized the chemical potential in terms of an electrical equivalence (Eq. (18)). Such a definition permits treatment of the circuit in terms of the standard circuit theory.

For the equivalent circuit of Fig. 2, the voltage drop across resistor R_i is given as

$$\Delta\tilde{\mu}_i^*(x,t) - \Delta\tilde{\mu}_i^*(x+\mathrm{d}x,t) = \Delta J_i^{\mathrm{charge}}(x,t) A R_i \tag{25}$$

The current flow along the displacement rail is described as

$$\Delta J_{\mathrm{dis}}^{\mathrm{charge}}(x,t) = \frac{C_{\mathrm{dis}}}{A}\frac{\partial}{\partial t}[\Delta\phi(x,t) - \Delta\phi(x+\mathrm{d}x,t)] \tag{26}$$

Applying Kirchoff's second law ($\Sigma J = 0$ at any branchpoint) to branchpoints A and E yields

$$\Delta J_i^{\mathrm{charge}}(x-\mathrm{d}x,t) - \Delta J_i^{\mathrm{charge}}(x,t) = \frac{C_i}{A}\frac{\partial}{\partial t}\Delta\mu_i^*(x,t) \tag{27}$$

These differential forms, Eqs. (25)–(27), can be rewritten as partial derivatives as

$$\Delta J_i^{\mathrm{charge}}(x,t) = -\frac{\mathrm{d}x}{A R_i}\frac{\partial}{\partial x}\Delta\tilde{\mu}_i^*(x,t) \tag{28}$$

$$\Delta J_{\mathrm{dis}}^{\mathrm{charge}}(x,t) = -\frac{C_{\mathrm{dis}}\,\mathrm{d}x}{A}\frac{\partial}{\partial t}\left[\frac{\partial}{\partial x}\Delta\phi(x,t)\right] \tag{29}$$

$$\frac{\partial}{\partial x}\left[\Delta J_i^{\mathrm{charge}}(x,t)\right] = -\frac{C_i}{A\,\mathrm{d}x}\frac{\partial}{\partial t}\Delta\mu_i^*(x,t) \tag{30}$$

This set of equations has exactly the form required by Eqs. (22)–(24). Thus, the proposed equivalent circuit indeed maps directly onto the physical reality, with the following correspondence between elements in the circuit and material properties:

$$R_i = \frac{1}{\sigma_i}\frac{\mathrm{d}x}{A} \tag{31}$$

$$C_{\mathrm{dis}} = \varepsilon_{\mathrm{r}}\varepsilon_0\frac{A}{\mathrm{d}x} \tag{32}$$

and

$$C_i = \frac{(z_i e)^2 c_i}{k_{\mathrm{B}}T} A\,\mathrm{d}x \tag{33}$$

It is then apparent that R_1 and R_2 are the resistances of carriers 1 and 2 of the element, respectively, whereas C_{dis} is the dielectric capacitance of the element. The quantities C_1 and C_2, discussed further below, are related to the "chemical capacitance," of the mixed conductor, as termed by Jamnik and Maier.[12] These capacitances represent the coupling between the multiple-current flow rails.

The equivalent circuit of Fig. 2 is greatly simplified if local electroneutrality is obeyed in the bulk. In this case,

$$ez_1\,\mathrm{d}c_1(x,t) + ez_2\,\mathrm{d}c_2(x,t) = 0 \tag{34}$$

and

$$ez_1\frac{\partial c_1(x,t)}{\partial t} + ez_2\frac{\partial c_2(x,t)}{\partial t} = 0 \tag{35}$$

In writing Eq. (34), an explicit account for the contribution of dopants to the charge distribution is not required because, as stated above, these species are taken to be immobile. Combining this with the continuity equation, Eq. (12), and noting that it is the perturbations in flux that are of interest, one obtains

$$\frac{\partial\Delta J_1^{\mathrm{charge}}(x,t)}{\partial x} + \frac{\partial\Delta J_2^{\mathrm{charge}}(x,t)}{\partial x} = 0 \tag{36}$$

This result implies that any flux flowing from carrier rail 1 to the displacement rail is exactly balanced by that flowing to the displacement rail from carrier rail 2. As a consequence, there is effectively no current flow between the carrier rails and the displacement rail (although flow between the two carrier rails remains possible). Accordingly, the circuit can be simplified to that shown in Fig. 3, by removing the electrical connection between the displacement rail and the two carrier rails. Doing so places C_1 and C_2 directly in series with one another (with no intervening branchpoints) and, thus, they can be combined into a single capacitance element defined according to the following equations:

$$C_{12} = \left(\frac{1}{C_1} + \frac{1}{C_2}\right)^{-1} = \frac{e^2}{k_{\mathrm{B}}T}\left(\frac{1}{z_1^2 c_1} + \frac{1}{z_2^2 c_2}\right)^{-1} A\,\mathrm{d}x \tag{37}$$

Because of the isolated flow along the carrier and displacement rails, each of the displacement capacitor elements is directly in series with one another and they can also be combined into one element:

$$C_{\mathrm{dis}}^{\mathrm{Total}} = \left(\int_0^L \frac{1}{C_{\mathrm{dis}}}\right)^{-1} = \left(\int_0^L \frac{\mathrm{d}x}{\varepsilon_{\mathrm{r}}\varepsilon_0 A}\right)^{-1} = \frac{\varepsilon_{\mathrm{r}}\varepsilon_0 A}{L} = C_{\mathrm{dielec}} \tag{38}$$

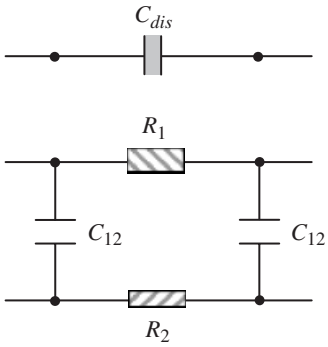

Fig. 3. Simplified differential element of the equivalent circuit of Fig. 2 under the additional condition of local charge neutrality. The capacitor C_{12} is a result of summing the capacitors C_1 and C_2 in series.

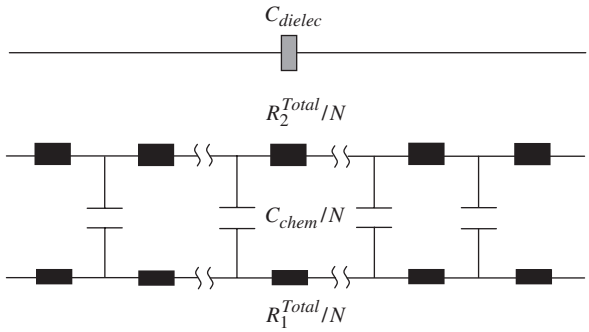

Fig. 4. Equivalent circuit for the entire material system obeying the current flow constraints Eqs. (22)–(24) and additionally obeying local charge neutrality.

where L is the length of the complete system. Thus, the capacitance along the displacement rail simply reduces to the conventional dielectric capacitance.

Although the resistances along the two carrier rails cannot be combined into single components, one can nevertheless define the total resistances encountered along these rails. They are given by

$$R_i^{\text{Total}} = \int_0^L R_i = \int_0^L \frac{\mathrm{d}x}{\sigma_i A} = \frac{L}{\sigma_i A} \tag{39}$$

which are the conventional resistance terms for the two species. Then the resistances of the differential circuit elements are

$$R_i = R_i^{\text{Total}} \frac{\mathrm{d}x}{L} = R_i^{\text{Total}}/N \tag{40}$$

where N is the (arbitrary) total number of differential subcircuits comprising the complete system. Because the resistance of an individual element cannot be measured, the superscript "Total" is, for notational simplicity, omitted hereafter, with the symbol R_i implying R_i^{Total}. One can similarly define a total chemical capacitance, C_{chem}, of the material system, which is simply the sum of all of the chemical capacitances of the differential portions of the circuit:

$$C_{\text{chem}} = \int_0^L C_{12} = \frac{e^2}{k_{\text{B}}T}\left(\frac{1}{z_1^2 c_1} + \frac{1}{z_2^2 c_2}\right)^{-1} AL \tag{41}$$

with

$$C_{12} = C_{\text{chem}} \frac{\mathrm{d}x}{L} = C_{\text{chem}}/N \tag{42}$$

describing the chemical capacitance of the element in the differential portion of the circuit. The equivalent circuit representing these relationships for the entire materials system (again, under conditions of time- and position-independent material properties) is shown in Fig. 4.

(C) Chemical Capacitance: The so-called chemical capacitance, C_{chem} [Eq. (41)], is a characteristic feature of the equivalent circuit of Fig. 4. As noted by Jamnik and Maier,[13] it is directly related to ambipolar diffusion in mixed conducting materials, where the ambipolar diffusion coefficient, $\tilde{D}$, is an aggregate diffusion coefficient describing the flux of matter through the system as a whole. Specifically, for a mixed conductor in which oxygen vacancies and electrons are mobile, the ambipolar or chemical diffusion coefficient relates the flux of neutral oxygen atoms to the gradient in the oxygen chemical potential in terms of Fick's first law.

To demonstrate the relationship between $\tilde{D}$ and C_{chem}, it is first useful to identify explicitly the two species in the system as the mobile ions and electrons, respectively. As in Jamnik and Maier,[13] the subscript "ion" is used here to indicate the ionic species and "eon" to indicate the electronic species. When the MIEC is subjected to a chemical potential gradient, both ion and electron transport occur in response. As given in Eq. (20), the charge flux because of ion motion is

$$\begin{aligned} J_{\text{ion}}^{\text{charge}}(x) &= -\sigma_{\text{ion}}(x)\frac{\partial \tilde{\mu}_{\text{ion}}^*(x)}{\partial x} \\ &= -\sigma_{\text{ion}}(x)\frac{\partial \mu_{\text{ion}}^*(x)}{\partial x} - \sigma_{\text{ion}}(x)\frac{\partial \phi(x)}{\partial x} \end{aligned} \tag{43}$$

Similarly, the charge flux because of electron motion is

$$\begin{aligned} J_{\text{eon}}^{\text{charge}}(x) &= -\sigma_{\text{eon}}(x)\frac{\partial \tilde{\mu}_{\text{eon}}^*(x)}{\partial x} \\ &= -\sigma_{\text{eon}}(x)\frac{\partial \mu_{\text{eon}}^*(x)}{\partial x} - \sigma_{\text{eon}}(x)\frac{\partial \phi(x)}{\partial x} \end{aligned} \tag{44}$$

In the absence of an external applied electrical potential gradient, ion and electron transport are coupled such that there is no net flux of charge, that is,

$$J_{\text{ion}}^{\text{charge}}(x) + J_{\text{eon}}^{\text{charge}}(x) = 0 \tag{45}$$

Combining Eqs. (43)–(45) yields

$$\begin{aligned} J_{\text{ion}}^{\text{charge}}(x) = &-\frac{\sigma_{\text{ion}}(x)\sigma_{\text{eon}}(x)}{\sigma_{\text{ion}}(x) + \sigma_{\text{eon}}(x)} \\ &\left[\frac{\partial \mu_{\text{ion}}^*(x)}{\partial x} - \frac{\partial \mu_{\text{eon}}^*(x)}{\partial x}\right] \end{aligned} \tag{46}$$

The bracketed term in Eq. (46) can be evaluated by noting that, from Eqs. (3) and (18), one obtains

$$\frac{\partial \mu_i^*(x)}{\partial x} = \frac{k_{\text{B}}T}{z_i e c_i(x)}\frac{\partial c_i(x)}{\partial x} \tag{47}$$

and that from the electroneutrality condition, Eq. (34), one obtains

$$z_{\text{ion}} e dc_{\text{ion}}(x) + z_{\text{eon}} e dc_{\text{eon}}(x) = 0 \tag{48}$$

Together, these imply

$$\begin{aligned} &\frac{\partial \mu_{\text{ion}}^*(x)}{\partial x} - \frac{\partial \mu_{\text{eon}}^*(x)}{\partial x} \\ &\quad = \frac{k_{\text{B}}T}{e^2} z_{\text{ion}} e\left[\frac{1}{z_{\text{ion}}^2 c_{\text{ion}}(x)} + \frac{1}{z_{\text{eon}}^2 c_{\text{eon}}(x)}\right]\frac{\partial c_{\text{ion}}(x)}{\partial x} \end{aligned} \tag{49}$$

In order to obtain a result in terms of a neutral oxygen atom concentration gradient and flux, it is necessary to note that mass balance (in terms of the total oxygen content of the system) implies that changes in the concentration of neutral oxygen atoms

must be balanced by changes in the concentration of oxygen vacancies and the fluxes must be similarly balanced. That is

$$dc_{ion}(x) + dc_O(x) = 0 \tag{50}$$

where c_O is the concentration of neutral oxygen atoms, and

$$J_{ion}^{mass}(x) + J_O^{mass}(x) = 0 \tag{51}$$

where J_{ion}^{mass} is the (mass) flux of neutral oxygen atoms. Using Eq. (50), it is possible to rewrite Eq. (49) in terms of the oxygen concentration gradient, whereas using Eqs. (51) and (11), it is possible to convert the charge flux of Eq. (46) into mass flux. The result is

$$J_O^{mass}(x) = -\frac{\sigma_{ion}(x)\sigma_{eon}(x)}{\sigma_{ion}(x)+\sigma_{eon}(x)}\frac{k_B T}{e^2} \times \left[\frac{1}{z_{ion}^2 c_{ion}(x)} + \frac{1}{z_{eon}^2 c_{eon}(x)}\right]\frac{\partial c_O(x)}{\partial x} \tag{52}$$

and the proportionality constant between J_O^{mass} and $\partial c_O/\partial x$ is the chemical or ambipolar diffusion coefficient, $\tilde{D}$. In a uniform chemical environment, the position dependence of the material properties can be ignored, yielding

$$\tilde{D} = \frac{\sigma_{ion}\sigma_{eon}}{\sigma_{ion}+\sigma_{eon}}\frac{k_B T}{e^2}\left(\frac{1}{z_{ion}^2 c_{ion}} + \frac{1}{z_{eon}^2 c_{eon}}\right) \tag{53}$$

This can be readily rewritten in terms of the total ionic and electronic resistances, Eq. (39), and the chemical capacitance, Eq. (41), to yield

$$\tilde{D} = \frac{L^2}{(R_{ion}+R_{eon})C_{chem}} \tag{54}$$

The chemical capacitance has certain similarities to conventional dielectric capacitance. While the latter is a measure of the ability of the system to store electrical energy in the form of polarized electric dipoles, the former is a measure of the ability of the system to store chemical energy in the form of changes in stoichiometry in response to changes in oxygen partial pressure. The analogy is made more explicit as follows: for a parallel plate capacitor with area A and length L, the conventional capacitance is

$$C_{dielec} = \frac{\partial q}{\partial \Delta\phi} = \frac{AD_{dis}}{EL} = \frac{A\varepsilon_r\varepsilon_0}{L} \tag{55}$$

where $D_{dis} = \varepsilon_r\varepsilon_0 E$ is the electrical displacement and E is the electrical field. In the case of chemical capacitance, the stored charge because of species i is

$$q_i = z_i e c_i AL \tag{56}$$

The voltage drop across the capacitor is μ_i^*(Fig. 2), defined previously as

$$\mu_i^* = \frac{\mu_i^0}{z_i e} + \frac{k_B T}{z_i e}\ln c_i \tag{57}$$

Defining the capacitance in analogy to Eq. (55) as $\partial q_i/\partial\mu_i^*$, and evaluating this quantity yield

$$C_{chem,i} = \frac{\partial q_i}{\partial \mu_i^*} = \frac{(z_i e)^2}{k_B T} c_i AL \tag{58}$$

which, as implied by Eq. (33), is the total chemical capacitance associated with species i. As suggested previously, with this definition, it is possible to view a battery, in which energy is stored chemically, as a chemical capacitor.[12] A thermodynamic interpretation of chemical capacitance has also been discussed.[22]

(D) Introduction of Electrodes: In a real system, the material under investigation is placed between electrodes, the properties of which establish the boundary conditions that apply to the flux terms of Eq. (17) (the displacement rail) and of Eq. (20) (the two carrier rails).[16] Treatment of this aspect of the overall problem via a first principles approach requires a detailed understanding of the electrochemical processes occurring at the electrode|electrolyte interface, at the electrode|gas interface, and within the electrode itself. Such an analysis is beyond the scope of the present work. In the simplest case, the electrodes are identical and, upon perturbation of the system, a step change in th concentration of species i across the electrode|electrolyte interface, Δc_i, is generated, and the resulting flux across that interface is proportional to Δc_i via a rate constant k_i. That is, $\Delta J_i^{mass} = \mp k_i \Delta c_i$ at $x = 0(-)$, $L(+)$. This behavior is equivalent to the assumption of Chang–Jaffé boundary conditions.[15,23] The expression can be converted into one relating charge flux to μ_i^* (the electrical equivalent of the chemical potential) using the definitions of Eqs. (11) and (18), and evaluating the differential of Eq. (2). The result is

$$\Delta J_i^{charge} = \mp\frac{(z_i e)^2 k_i c_i}{k_B T}\Delta\mu_i^* \tag{59}$$

where the minus sign applies at $x = 0$ and the plus sign applies at $x = L$. In the terminology of Fig. 2, this corresponds to the behavior of a simple resistor that connects each of the carrier rails to the displacement rail and has resistance

$$R_i^{\perp} = \frac{k_B T}{(z_i e)^2 k_i c_i} \tag{60}$$

where the superscript $\perp$ indicates the properties of the interface (with charge flow occurring perpendicular to that interface).

The flux across the electrode|electrolyte interface must be exactly equal to that which travels through the carrier rails, and thus, the $R_i^{\perp}$ resistors are in series with the R_i terms of the MIEC. Under the (perhaps unrealistic) assumptions of Chang–Jaffé boundary conditions, there is no capacitance explicitly due to the interface, and the displacement rail should be directly connected to the terminal voltage.[16] If, however, one wishes to introduce interfacial capacitive effects, this can be done by replacing the interfacial resistors with parallel RC circuits (one for each of the two species). In combination with the circuit of Fig. 4, the complete system including the electrodes is then represented as in Fig. 5. The area-specific electrode resistance is $\rho_{ion}^{\perp} = R_{ion}^{\perp} A$. Although it needs to be emphasized that electrodes in the most general case cannot be described by this simple representation, this model, as discussed below, yields

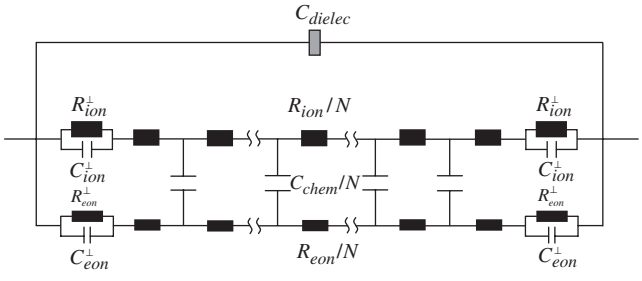

Fig. 5. Equivalent circuit for a system comprised of an mixed ionic and electronic conductors (MIEC) placed between two electrodes. R_{ion}, R_{eon}, and C_{chem} refer to the ionic resistance, electronic resistance, and chemical capacitance of the MIEC, which are weighted by $1/N$, N being the number of transmission line elements, in turn, defined as $N = L/\Delta x$, where L is the sample thickness and Δx is the element thickness. $R_{ion}^{\perp}$, $R_{eon}^{\perp}$, $C_{ion}^{\perp}$, and $C_{eon}^{\perp}$ refer to ionic and electronic resistances and capacitances of the electrodes. C_{∞} is the bulk, dielectric capacitance of the MIEC.

an impedance that fits the experimental data obtained from the Pt|ceria|Pt system exceptionally well. Finally, it must be noted that Maya *et al.*[14] have attempted a similar analysis, in which the flux equations for a system with multiple charged carriers are mapped to an equivalent circuit representation. The formalism used in that work does not lend itself to a straightforward comparison with the work of Jamnik and Maier, although it does appear that the two sets of results differ, possibly because of the different boundary conditions used.

(E) Impedance Evaluation: The analytical expression for the impedance of the circuit of Fig. 5 has been given by Jamnik and Maier,[13] and is derived here in Appendix A. As in that work, for the remainder of the discussion, the impact of the bulk dielectric capacitance, C_{dielec}, on the impedance response is omitted for clarity. This element simply adds impedance $1/j\omega C_{\text{dielec}}$, where ω is the frequency and j is $\sqrt{-1}$, to the total impedance of the system. Because C_{dielec} is typically small, it affects the impedance spectrum only at high frequencies, in most cases beyond the high-frequency measurement limit. The result (corrected with respect to a typographical omission of the term $(Z_0 - Z_\infty)$ in Eq. (7) of Jamnik and Maier[13]) is

$$Z(\omega) = Z_\infty + (Z_0 - Z_\infty) \times \frac{\tanh\sqrt{\frac{j\omega L^2}{4\tilde{D}}} + \frac{R_{\text{ion}}+R_{\text{eon}}}{2\left(Z^{\perp}_{\text{ion}}+Z^{\perp}_{\text{eon}}\right)}\tanh\sqrt{\frac{j\omega L^2}{4\tilde{D}}}}{\sqrt{\frac{j\omega L^2}{4\tilde{D}}} + \frac{R_{\text{ion}}+R_{\text{eon}}}{2\left(Z^{\perp}_{\text{ion}}+Z^{\perp}_{\text{eon}}\right)}\tanh\sqrt{\frac{j\omega L^2}{4\tilde{D}}}} \tag{61}$$

$$\frac{1}{Z_0} = \frac{1}{R_{\text{ion}} + 2Z^{\perp}_{\text{ion}}} + \frac{1}{R_{\text{eon}} + 2Z^{\perp}_{\text{eon}}} \tag{62}$$

$$Z_\infty = \frac{R_{\text{ion}}R_{\text{eon}}}{R_{\text{ion}} + R_{\text{eon}}} + 2\frac{Z^{\perp}_{\text{ion}}Z^{\perp}_{\text{eon}}}{Z^{\perp}_{\text{ion}} + Z^{\perp}_{\text{eon}}} \tag{63}$$

$$Z^{\perp}_{\text{ion}} = \frac{R^{\perp}_{\text{ion}}}{1 + j\omega R^{\perp}_{\text{ion}}C^{\perp}_{\text{ion}}} \tag{64}$$

$$Z^{\perp}_{\text{eon}} = \frac{R^{\perp}_{\text{eon}}}{1 + j\omega R^{\perp}_{\text{eon}}C^{\perp}_{\text{eon}}} \tag{65}$$

Jamnik and Maier[13] have shown that this impedance adequately reproduces the exact impedance of an electrode|MIEC|electrode system with Chang–Jaffé boundary conditions,[15] as long as the sample thickness, L, is significantly longer than the Debye length $L_D = \sqrt{\varepsilon_r\varepsilon_0 k_B T/\sum_i (z_i e)^2 c_i}$, of the MIEC|electrode interface. Specifically, the error is typically less than a fraction of a percent for $L > \sim 10^4 L_D$. At small distances, space charge effects become significant, violating the approximation of local electroneutrality, and thus the displacement rail can no longer be disconnected from the carrier rails.

Plotted in the complex plane (i.e., in Nyquist form), the impedance of the circuit in Fig. 5 has the general appearance of a single arc that is displaced from the origin (along the real axis of Z), examples of which are shown in Fig. 6. The offset along the real axis translates into a high-frequency arc if the dielectric capacitance is accounted for. An important feature of the electrode|MIEC|electrode system is that for a wide range of material properties, the low-frequency arcs exhibits a characteristic, half tear-drop shape with a straight line at its high-frequency side, as shown in Fig. 6(a). Historically, this feature has been associated with diffusion-controlled processes at the electrodes.[8] What is unusual here is that this impedance response is apparently an almost default feature of mixed conducting electrolytes; it does not require diffusion- and/or adsorption-limited processes at the electrodes, nor does it require any particular chemical behavior within the bulk of the MIEC. If the material is truly a mixed conductor, with $c_{\text{ion}} \sim c_{\text{eon}}$ and $D_{\text{ion}} \sim D_{\text{eon}}$, symmetric arcs as in Fig. 6(b) will result only if the electrodes are not selective (meaning $R^{\perp}_{\text{ion}} \sim R^{\perp}_{\text{eon}}$). More typically, symmetric

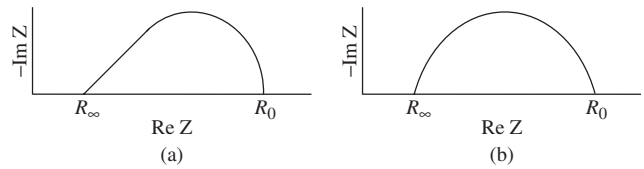

Fig. 6. Schematic Nyquist plots resulting from the circuit in Fig. 5 representing a metal|MIEC (mixed ionic and electronic conductors)|metal system. (a) Asymmetric, half tear-drop-shaped arcs result when the rates of transport of the two species across the MIEC|electrode interface are dissimilar. (b) Symmetric, semi-circular arcs result when the rates are comparable.

arcs result when there is only one mobile species, i.e., the material is no longer a mixed conductor. Under highly unusual circumstances (not considered here further), an additional arc can appear at intermediate frequencies.[13]

Graphical analyses of the types of spectra that result under certain limiting conditions from the impedance expressed in Eq. (61) have been presented by Jamnik and Maier, but without analogous explicit expressions for $Z(\omega)$ or physical interpretation of the characteristic parameters of these spectra. Interpretation of the intercepts of the impedance spectra with the real axis, labeled R_∞ and R_0 in Fig. 6, can be achieved by evaluation of the high- and low-frequency limits of the circuit of Fig. 5. At the high-frequency limit, all of the capacitors are effectively shorted ($Z_{\text{capacitor}} = 1/j\omega C \to 0$), producing the circuit shown in Fig. 7(a). The electrode resistance to charge transfer effectively disappears, and the impedance in this limit is $Z(\omega \to \infty) = R_\infty$. Thus, the high-frequency intercept corresponds to the total electrical resistance of the MIEC that results from adding the electronic and ionic components, R_{eon} and R_{ion}, in parallel, with

$$\frac{1}{R_\infty} = \frac{1}{R_{\text{ion}}} + \frac{1}{R_{\text{eon}}} \tag{66}$$

At the low-frequency limit, all of the capacitors are effectively open ($Z_{\text{capacitor}} = 1/j\omega C \to \infty$), producing the circuit shown in Fig. 7(b). The impedance in this limit, $Z(\omega \to 0) = R_0$, can be immediately determined from the circuit to obey

$$\frac{1}{R_0} = \frac{1}{R_{\text{ion}} + 2R^{\perp}_{\text{ion}}} + \frac{1}{R_{\text{eon}} + 2R^{\perp}_{\text{eon}}} \tag{67}$$

In this case, the intercept corresponds to the electrical resistance of the system as a whole, and is the value that results from first adding the two ionic components together in series, similarly adding the two electronic components together in series, and then adding these two composite terms together in a parallel fashion.

Two features of R_0 and R_∞ are noteworthy. First, in the case of a perfectly ion-blocking electrode ($R^{\perp}_{\text{ion}}, Z^{\perp}_{\text{ion}} \to \infty$), with perfect reversibility for electrons ($R^{\perp}_{\text{eon}}, Z^{\perp}_{\text{eon}} = 0$), R_0 reduces to R_{eon}, which is precisely how one obtains the electronic component of the conductivity of a MIEC using blocking electrodes. Second, the difference between R_0 and R_∞ does not, in the general case, equate to the resistance of the electrodes, as it would in the case of an purely ionically conducting electrolyte. Instead,

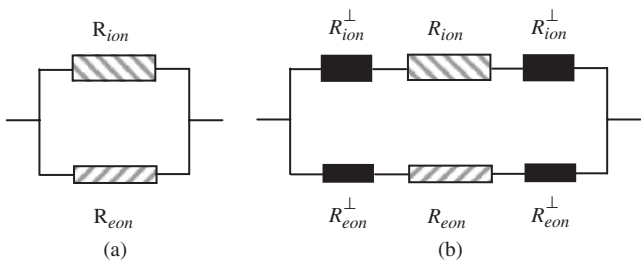

Fig. 7. Equivalent circuits representing that of Fig. 5 in (a) the high-frequency limit in which all capacitors are shorted, and (b) the low-frequency limit in which all capacitors are open.

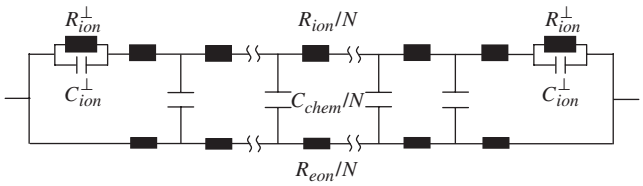

Fig. 8. Equivalent circuit for the metal|ceria|metal system assuming metal electrodes that are ideally reversible for electrons ($R_{\text{eon}}^{\perp}, Z_{\text{eon}}^{\perp} = 0$). The analytical expression for the impedance of this circuit is given in Eq. (68).

because R_0 depends on all four resistance terms of the system, further analysis, as described below, must be performed in order to extract the electrode resistance from the impedance data.

With this background, it is possible to consider the specific situation for ceria placed between two metal electrodes. If the electrodes are perfectly reversible to electrons and partially blocking to oxygen ions, then $R_{\text{eon}}^{\perp} = 0$, whereas $R_{\text{ion}}^{\perp}$ and $C_{\text{ion}}^{\perp}$ have finite values. Under these conditions, the equivalent circuit of Fig. 5 is reduced to that given in Fig. 8, and its impedance reduces to

$$Z(\omega) = R_{\infty} + (Z_0 - R_{\infty}) \times \frac{\tanh\sqrt{\frac{j\omega L^2}{4\tilde{D}}} + \frac{R_{\text{ion}}+R_{\text{eon}}}{2Z_{\text{ion}}^{\perp}}\tanh\sqrt{\frac{j\omega L^2}{4\tilde{D}}}}{\sqrt{\frac{j\omega L^2}{4\tilde{D}}} + \frac{R_{\text{ion}}+R_{\text{eon}}}{2Z_{\text{ion}}^{\perp}}\tanh\sqrt{\frac{j\omega L^2}{4\tilde{D}}}} \tag{68}$$

where

$$R_{\infty} = \frac{R_{\text{ion}}R_{\text{eon}}}{R_{\text{ion}} + R_{\text{eon}}} \tag{69}$$

and Z_0 reduces to

$$\frac{1}{Z_0} = \frac{1}{R_{\text{ion}} + 2Z_{\text{ion}}^{\perp}} + \frac{1}{R_{\text{eon}}} \tag{70}$$

The low-frequency intercept similarly reduces to

$$\frac{1}{R_0} = \frac{1}{R_{\text{ion}} + 2R_{\text{ion}}^{\perp}} + \frac{1}{R_{\text{eon}}} \tag{71}$$

While Eq. (68) has been used here for the analysis of the metal|ceria|metal system, it is noteworthy that under certain conditions, further simplifications occur. If C_{chem} is substantially larger than $C_{\text{ion}}^{\perp}$, then, $C_{\text{ion}}^{\perp}$, can be ignored in the overall equivalent circuit ($Z_{\text{ion}}^{\perp} \rightarrow R_{\text{ion}}^{\perp}$) and the impedance becomes

$$Z(\omega) = R_{\infty} + (R_0 - R_{\infty}) \times \frac{\tanh\sqrt{\frac{j\omega L^2}{4\tilde{D}}} + \frac{R_{\text{ion}}+R_{\text{eon}}}{2R_{\text{ion}}^{\perp}}\tanh\sqrt{\frac{j\omega L^2}{4\tilde{D}}}}{\sqrt{\frac{j\omega L^2}{4\tilde{D}}} + \frac{R_{\text{ion}}+R_{\text{eon}}}{2R_{\text{ion}}^{\perp}}\tanh\sqrt{\frac{j\omega L^2}{4\tilde{D}}}} \tag{72}$$

where R_{∞} and R_0 are as given in Eqs. (69) and (71). If, in addition, the resistance of the electrodes to ion transfer is high (i.e., ion blocking) such that $2R_{\text{ion}}^{\perp} \gg R_{\text{ion}} + R_{\text{eon}}$, Eq. (72) is still further reduced to

$$Z(\omega) = R_{\infty} + (R_0 - R_{\infty})\frac{\tanh\sqrt{\frac{j\omega L^2}{4\tilde{D}}}}{\sqrt{\frac{j\omega L^2}{4\tilde{D}}}} \tag{73}$$

where R_{∞} is unchanged and R_0 is equal to R_{eon}. The second term of this result has the same mathematical form as the well-known finite-length Warburg impedance.[24]

The equivalent circuit of Fig. 5 applies to a system in which a single step dominates the entire electrochemical reduction/oxidation reaction. In many cases, however, multiple sequential steps with differing time constants contribute to the overall process. Ideally, the impedance spectra yield detailed information regarding each of these reaction steps. In the present system, however, because $C_{\text{chem}} \gg C_{\text{ion}}^{\perp}$, the parallel resistor and capacitor of the electrode impedance to ion transfer can readily be approximated as a simple resistor (that is, $C_{\text{ion}}^{\perp} \sim 0$). Thus, the possible presence of additional parallel *RC* subcircuits that are in series with one another cannot be observed; each *RC* subcircuit reduces to a resistor, and simple resistors in series cannot be individually measured. Electrode processes at the interface with an MIEC are thus inherently masked by the material's large chemical capacitance. This behavior is quite distinct from that of pure ionic conductors, in which multiple electrode arcs are routinely observed, and their presence is used to probe complex reaction pathways.[25]

From the impedance analysis of an MIEC with electron-reversible electrodes, one can, according to Eq. (68), determine five independent material parameters: the bulk ionic and electronic resistances (R_{ion} and R_{eon}), the interfacial capacitance $C_{\text{ion}}^{\perp}$ and resistance $R_{\text{ion}}^{\perp}$ of the electrodes to ion transfer, and the chemical diffusion coefficient $\tilde{D}$. With these data in hand, one can then make use of Eq. (54) to determine the value of the chemical capacitance, C_{chem}. If, in addition, the concentration of the majority carriers (c_{ion}) is given from the material stoichiometry (i.e., extrinsic dopant concentration), one can use the definition of the chemical capacitance, Eq. (41), to evaluate the concentration of minority carriers (c_{eon}). With both the resistances and concentrations of the mobile species known, one can then even establish the mobilities. In this manner, it is possible to characterize completely the electrical properties of MIECs simply from the measurement of AC impedance spectra.

In practice, directly fitting the impedance data to Eq. (68) is difficult. The two resistance terms, R_{∞} and R_0, which capture the essential features of the impedance spectrum are, as, respectively, defined in Eqs. (69) and (71), composite terms of the material parameters. As a consequence, the material parameters derived are highly correlated, and the refinement can easily fall into false local minima. A strategy for addressing this limitation is outlined below as part of the experimental procedure implemented in the present study. The key to the success of this strategy is the measurement of the impedance response over a broad range of oxygen partial pressures.

(F) Influence of Grain Boundaries: A complete description of the impedance response of ceria requires, in principle, a model for the transport of ions and electrons through the grain boundary regions. For samples with typical, micron-scale grains placed under moderately oxidizing conditions (where acceptor-doped ceria is a pure ionic conductor), it has been observed that the grain boundaries, because they are depleted of oxygen vacancies, serve as barriers to ion transport. In the case of 10% Y-doped ceria, for example, the grain boundary activation energy is 1.02 eV as compared with 0.97 eV for the bulk.[26] Enhanced grain boundary resistance becomes more severe if samples are processed at high temperatures at which impurity segregation to grain boundaries can occur.[27] Accordingly, the impedance spectrum in the high-frequency regime exhibits two arcs: one deriving from the bulk (grain interior or lattice) properties, and one from the (serial or perpendicular) grain boundaries. The depletion of oxygen vacancies at grain boundaries is accompanied by an enhancement in the free electron carrier concentration and, in the case of ceria with nanometer-scale grains, the space charge region of enhanced electronic conductivities deriving from grain boundaries on opposing sides of the grains can overlap. As a consequence, the entire material can show enhanced conductivity because of electron transport, even though the environmental conditions would normally render the material a pure ionic conductor. In such an event, only one arc is observed in the impedance spectrum. These effects have now been documented by several workers, and the origins have been understood to some extent.[28,29] A theoretical analysis of the impact of ion-blocking grain boundaries on the impedance of MIECs has recently been presented by Jamnik,[30] and a first set of experimental studies has been carried out by Jasinski *et al.*[27]

In the present study, grain boundary effects are not treated for the primary reason that they are not observed in the experimental data. This is because sample processing has been carried out by conventional routes that do not lead to nanostructured grains and at moderate sintering temperatures such that dopant (and impurity) segregation is minimized. Thus, anomalous conductivity enhancement does not occur and grain boundaries are more resistive than the grain interiors but not dramatically so. Furthermore, because of the higher activation energy associated with ion transport across grain boundaries than through grains, the resistance because of grain boundaries falls more rapidly as the temperature is increased than that because of the bulk.[27] Consequently, at the moderately high temperatures of the present studies, the grain boundary contribution to R_∞ can be safely ignored. At lower temperatures (or somewhat smaller grain sizes), approximating R_{bulk} by R_∞ is no longer justified and a clear grain boundary arc becomes visible in the data. Treatment of this much more complex situation is beyond the scope of the present work, and, as already stated, not relevant to the experimental conditions used.

(G) Alternative Approaches: The Finite-Length Warburg and Gerischer Elements: It is widely recognized that a diffusion-limited process can lead to an impedance response in the Nyquist representation that appears as a straight line with a 45° slope at the high-frequency side and a semi-circular arc at its low-frequency side, that is, has a half tear-drop shape. Several authors have derived an impedance of a general functional form[24]for specific situations

$$Z_W(\omega) = Z_W(0)\frac{\tanh\sqrt{j\Lambda}}{\sqrt{j\Lambda}} \tag{74}$$

where Λ is a dimensionless quantity proportional to ω, to describe this observed response.

A typical derivation of this finite-length Warburg type of response applies to a supporting electrolyte placed between kinetically reversible electrodes,[24] a case more often encountered in liquid rather than solid electrolytes, but nevertheless illustrative. The physical situation is as follows; the electrodes are perfectly reversible to the transport of one type of charge carrier and entirely blocking to all others. Within the electrolyte, the mobility and concentration of the blocked species approach infinity (hence the electrolyte is supported), whereas the conductivity of the non-blocked species is finite, and is typically the quantity to be determined from the impedance measurement. For a liquid electrolyte, both blocked (i.e., supporting) and non-blocked species are typically ions, whereas for solids electronic carriers (electrons or holes) may constitute one of even both of the species. In such a supported electrolyte (or mixed conductor), the internal electric field gradient is zero as a consequence of the rapid response of the supporting species. Thus, the diffusion–drift equation reduces to Fick's first law; the continuity equation, again in the absence of sources or sinks, to Fick's second law; and the displacive flux (Eq. (17)) because of Poisson's equation becomes zero. The diffusion coefficient here is the self-diffusion coefficient of the species of interest (D_i) as this property approximates the chemical diffusion coefficient ($\tilde{D}$) when the mobility and concentration of the partner species are very large (Eq. (53)). One can then solve for the time-dependent charge flux and apply the boundary conditions implied by the blocking/non-blocking behavior of the electrodes to obtain the result[24]

$$Z(\omega)A = \frac{2k_BT}{z_{\text{ion}}^2e^2c_{\text{ion}}(j\omega D_{\text{ion}})^{0.5}}\tanh[(j\omega/D_{\text{ion}})^{0.5}(L/2)] \tag{75}$$

From the perspective of the equivalent circuit presented in Fig. 5, a similar result can be readily obtained. Taking the bulk electronic resistance to be zero ($R_{\text{eon}} \to 0$) [that is, the electrons are the supporting species], the resistance to electron transfer across the electrode|MIEC interface to be infinity ($Z_{\text{eon}} \to \infty$), and the resistance to ion transfer across the interface to be zero ($Z_{\text{ion}} \to 0$), the circuit reduces to that shown in Fig. 9. Inserting these limiting values into Eq. (61) yields the impedance

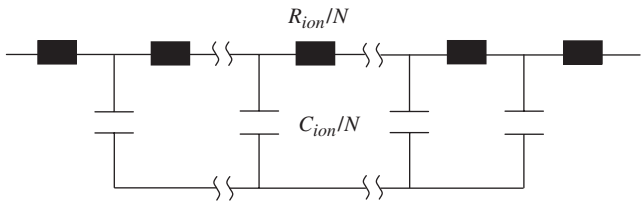

Fig. 9. Equivalent circuit of an ideally supported mixed conductor ($R_{\text{eon}} \to 0$ placed between identical, ideally selective electrodes ($Z^{\perp}_{\text{ion}} \to 0$ and $Z^{\perp}_{\text{eon}} \to \infty$).

$$Z(\omega) = R_{\text{ion}}\frac{\tanh\sqrt{j\omega L^2/4\tilde{D}}}{\sqrt{j\omega L^2/4\tilde{D}}} \tag{76}$$

which is identical in form to Eq. (75). The exact equivalence between Eqs. (75) and (76) can be established by converting from R_{ion} to σ_{ion} and making use of the Nernst–Einstein relation, Eq. (5).

Explicit assignment of impedance values to the electrode processes provides a means of revealing boundary conditions that are implicitly applied at the sample|electrode interfaces. For example, in their treatment of a supported electrolyte, Franceschetti *et al.*[24] state that the voltage V across the system can be described by Nernst's equation:

$$\Delta V = \frac{k_BT}{z_ie}\Delta\ln c_i \tag{77}$$

implying that there are no additional voltage drops because of the properties of the interface or of the electrodes. According to the Jamnik–Maier model, this is to say that the electrodes are perfectly reversible to the non-blocked species, and perfectly blocking to the supporting species.

In another example, Bisquert[31] has treated the problem of electron diffusion in a semiconductor, where holes are the supporting species. The physical situation is asymmetric, unlike the cases considered above, and the two boundaries of the semiconductor are treated separately. At one boundary, the flux is taken to be given by Fick's first law (as applied to electrons). Such a statement, in fact, implies that the electrode at this boundary is ideally reversible to electrons and apparently implies that the boundary is also ideally blocking to holes. The opposite boundary is taken either to be (i) absorbing of the electrons, such that they traverse the boundary unimpeded, or (ii) reflecting of the electrons, such that they cannot traverse it. These boundary conditions immediately correspond to (i) electrodes that are kinetically reversible to electrons, and (ii) electrodes that are ideally blocking to electrons. Also, it is apparently implied that the electrodes at this boundary are ideally reversible to holes (for both reflecting and absorbing boundary conditions). The final result for the absorbing boundary condition is a finite-length Warburg impedance of a general form as given in Eq. (74). For the reflecting boundary condition, the impedance has the general form

$$Z_W(\omega) = Z_W(0)\frac{\coth\sqrt{j\Lambda}}{\sqrt{j\Lambda}} \tag{78}$$

Again, each of these results can be directly obtained from the Jamnik–Maier formalism simply by applying the appropriate values to the electrode properties.

It is to be noted that, as indicated by Eq. (75), the tear-drop-shaped impedance arc that results from a supported mixed conductor is not displaced from the origin because the high mobility

of the electrons precludes any high-frequency capacitive effects. Furthermore, the low-frequency intercept directly yields the bulk resistance to ion transport. Overall, the impedance data contain no information regarding the behavior of the electrodes as these were, *a priori*, taken to be ideally reversible with respect to ions and ideally blocking with respect to electrons.

An example of a case where the electrolyte is not fully supported, that is, the conductivity of the partner species is not infinite, has already been treated here via the Jamnik–Maier approach in the discussion surrounding the specific case of ceria placed between two metal electrodes. An identical result can be obtained using an analytical method analogous to that described above for the treatment of a supported electrolyte. In this case, however, the internal field is not zero. Consequently, the drift–diffusion and continuity equations must be used in full (although, again, sources and sinks are taken to be absent in writing down the latter) and must be applied to both species. The equations cannot be approximated by Fick's laws. In addition, one must also take into account the displacement flux resulting from Poisson's equation. One then again solves for the time-dependent flux using the relevant boundary conditions: electrodes that are ideally blocking to one of the species and ideally reversible to the other. Franceschetti *et al.*[24] have applied this approach to the specific case in which the magnitude of the charge of the two species is the same and obtained the result

$$Z(\omega)A = \frac{k_B T L}{z_2^2 e^2 c_2 (D_1 + D_2)} + \frac{4 t_1^2 k_B T}{z_2^2 e^2 c_2 (j\omega \tilde{D})^{0.5}} \tanh[(j\omega/\tilde{D})^{0.5}(L/2)] \quad (79)$$

where species 1 is that which is blocked at the electrodes (species 2 is unimpeded) and t_i is the transference number, defined as $t_i = \sigma_i / \sum \sigma_i$. The situation directly corresponds to that described by Eq. (73), with the exception that the vacancies and electrons in ceria have differing magnitudes of charge. Using the Jamnik–Maier formalism, it is straightforward to obtain the result for the more general case, and, again, there is a quantitative correspondence between the approaches. Specifically, the equivalence of the first terms in Eqs. (73) and (79) can be established by again converting from R_i to σ_i, making use of the Nernst–Einstein relation, Eq. (5), and now also taking into the account the assumption of local electroneutrality. That is, $z_1 c_1 = z_2 c_2$, which, for a material where $z_1 = z_2$, also implies $c_1 = c_2$. Establishing the equivalence of the second terms in Eqs. (73) and (79) requires, in addition to these steps, use of the definition of the chemical diffusion coefficient, as given in Eq. (53). It is to be emphasized that, once again, no information is available about the electrode properties from the impedance spectrum of this type of system as the electrodes are *a priori* assumed to behave ideally.

Of course, there is much to be learned about electrodes from AC impedance spectroscopy, and the above statements regarding systems with ideal electrodes are not meant to imply otherwise. A mixed conducting electrode can be treated straightforwardly by applying asymmetric boundary conditions, in analogy to the situation described by Bisquert[31] for semiconductor materials. A specific example of interest to the solid-state ionics community, that of (La,Sr)$CoO_{3-\delta}$ on YSZ, has been explicitly treated by Jamnik and Maier[12] and used to explain the observed experimental results.

Up to this point in the discussion, the possibility of internal reactions that either generate or consume mobile species has not been considered. That is, the continuity equation, Eq. (8), has been written down without regard to potential sources or sinks. In principle, it is possible to account for such effects by adding a term with the form $k_i^r \Delta c_i$ to the continuity equation, where k_i^r is a first-order rate constant for an irreversible reaction. Bisquert[31] has pursued this approach to describe electron–hole pair annihilation in a semiconductor material, under the implicit assumption of a supported "electrolyte" in which there is no internal field. Of greater relevance to the solid-state ionics community is the treatment of Boukamp[7] of heavily Tb-doped YSZ, a mixed conductor. Here again, the material is implicitly assumed to be entirely supported (that is, the internal field is zero and the migration term in the diffusion–drift equation is neglected) and an additional source term of the form $k_i^r \Delta c_i$ is added to Fick's second law, yielding the relevant continuity equation. As in the case of the supported electrolyte without sources or sinks, one can then solve for the time-dependent charge flux and apply the relevant boundary conditions. Both Bisquert[31] and Boukamp and Bouwmesster[7] show that from an equivalent circuit perspective, the source/sink introduces resistors in parallel with each of the chemical capacitors of Fig. 2. The resulting impedance (correcting by a factor of two from that derived by Boukamp[‡]) is

$$Z(\omega)A = \frac{2 k_B T}{z_{ion}^2 e^2 c_{ion}} \frac{\tanh\left[(L/2)\sqrt{(j\omega + k_{ion}^r)/D_{ion}}\right]}{\sqrt{(j\omega + k_{ion}^r) D_{ion}}} \quad (80)$$

(for an ideal solution in which Eq. (2) applies). This impedance clearly reduces to that given in Eq. (75) if $k_{ion}^r \to 0$. In addition, for $D_{ion} \ll L^2 k_{ion}^r$, Eq. (80) reduces to a form in which the impedance is proportional to $(k+jw)^{-0.5}$. This type of impedance (e.g., $Z(\omega) \sim (k+jw)^{-0.5}$) is often termed the Gerischer impedance, after the author who first derived it in 1951.[11] While the result as given by Boukamp applies when the reaction occurs within the bulk of the MIEC,[6,7] such behavior also results when the electrode reactions are "co-limited" by diffusion and reaction.[8]

In the present study, the possibility that some internal reaction might modify the continuity equation has not been explicitly examined. Boukamp has suggested that in Tb-YSZ, the source term might correspond to the release of oxygen vacancies otherwise trapped at dopant sites.[6,7] Defect trapping in ceria occurs at temperatures lower than those at which the material has been studied here.[18] Furthermore, and perhaps more significantly, it is difficult to imagine an internal process in an ionic material that generates or consumes mobile species at a constant rate. Such a concern does not arise for semiconductors in which electron–hole pair annihilation/generation can be balanced by the input or removal of energy from the system. Finally, it is noteworthy that for the present material, treatment of internal reactions by modification of the continuity equation requires that this be done while retaining the effect of an internal electrical field. In principle, such a treatment (which has not yet appeared in the literature) is possible, but is beyond the scope of the present study.

(2) Defect Chemistry and Electrical Properties of Doped Ceria

While the defect behavior of mixed conductors has been described in several texts,[32,33] the equations relevant to the specific situation of ceria under mildly reducing conditions are briefly reviewed here for completeness. The reduction reaction of ceria, involving the loss of oxygen and a change in the cerium oxidation state from 4+ to 3+, can be written as

$$O_O^\times \leftrightarrow \tfrac{1}{2}O_2 + V_O^{\bullet\bullet} + 2Ce'_{Ce} (2e') \quad (81)$$

where the Kröger–Vink notation has been used, and $[V_O^{\bullet\bullet}]$ and $n = [e']$ are the concentrations of oxygen vacancies and electrons, respectively. The equilibrium constant, K_r, associated with this reaction is

$$K_r = [V_O^{\bullet\bullet}] n^2 p_{O_2}^{1/2} \quad (82)$$

In the ionic regime of doped ceria, the concentration of electronic charge carriers is negligible and the concentration of oxygen ion vacancies fixed by the acceptor dopant concentration

[‡]Boukamp and Bouwmeester[7] define the relevant voltage drop in Eq. (5) of as that at only one of the electrode/electrolyte intefaces. In fact, the total voltage drop across both interfaces is the relevant quantity.

according to $[V_O^{\bullet\bullet}] = 1/2[Sm'_{Ce}]$. Consequently, the total conductivity (essentially equal to the ionic conductivity) is independent of oxygen partial pressure. Under slightly more reducing conditions, although the fixed concentration of oxygen vacancies may still be far greater than the concentration of mobile electrons, the concentration of the latter becomes significant enough to impact the total conductivity. Combining the fixed vacancy concentration with the equilibrium constant, Eq. (82), yields

$$n = \left(\frac{2K_r}{[Sm'_{Ce}]}\right)^{1/2} p_{O_2}^{-1/4} \tag{83}$$

from which one obtains the well-known $-1/4$ power law for the dependence of electronic conductivity on oxygen partial pressure. The total conductivity, σ_T (the sum of the ionic, σ_{ion}, and electronic, σ_{eon}, conductivities), thus exhibits a oxygen partial pressure dependence given as

$$\sigma_T = \sigma_{ion} + \sigma_{eon} = \sigma_{ion} + \sigma^0_{eon} p_{O_2}^{-1/4} \tag{84}$$

where σ_{ion} and σ^0_{eon} are independent of oxygen partial pressure, and they are, respectively, defined as

$$\sigma^0_{eon} = eu_{eon}\left(\frac{2K_r}{[Sm'_{Ce}]}\right)^{1/2} \tag{85}$$

and

$$\sigma_{ion} = eu_{ion}[Sm'_{Ce}] \tag{86}$$

where $u_{ion}$and u_{eon} denote ionic and electronic mobilities, respectively. From a plot of conductivity as a function of oxygen partial pressure, one can, by fitting to Eq. (84), determine the ionic and electronic conductivities over the entire p_{O_2} regime of interest, and such measurements are performed relatively routinely.[34–36]

Under the conditions of a fixed oxygen vacancy concentration (as considered here), the temperature dependence of the ionic conductivity derives from the temperature dependence of the ionic mobility :

$$u_{ion} = \frac{v_{ion}}{T}\exp\left(-\frac{\Delta H_{ion}}{k_B T}\right) \tag{87}$$

where v_{ion} is a constant and ΔH_{ion} is the activation energy for ion migration. Thus, an Arrhenius plot of the ionic conductivity directly yields ΔH_{ion} from its slope.

The electronic mobility exhibits a temperature dependence analogous to Eq. (87). However, because the concentration of mobile electrons, Eq. (83), depends on temperature via the temperature dependence of K_r, the activation energy for electron migration cannot be immediately evaluated. Specifically, K_r depends on temperature according to

$$K_r = \exp\left(\frac{\Delta S_r}{k_B}\right)\exp\left(-\frac{\Delta H_r}{k_B T}\right) \tag{88}$$

where ΔS_r and ΔH_r are, respectively, the reduction entropy and enthalpy of reaction (81). Then, temperature dependence of σ^0_e is

$$\begin{aligned}\sigma^0_{eon} &= \frac{w_{eon}}{T}\exp\left(-\frac{\Delta H_{eon,o}}{k_B T}\right)\\ &= \frac{w_{eon}}{T}\exp\left[-\frac{(\Delta H_{eon} + 1/2\Delta H_r)}{k_B T}\right]\end{aligned} \tag{89}$$

where w_{eon} is a constant, and σ^0_{eon} exhibits an apparent, or combined, activation energy of $\Delta H_{eon,o} = \Delta H_{eon} + 1/2\Delta H_r$. It is thus not generally possible to determine independently the migration and reduction enthalpies (or, more broadly, the mobility and concentration) of electronic defects from a measurement of MIEC conductivity even over wide temperature and oxygen partial pressure ranges. It is shown below, however, that one can obtain the electronic defect concentration from a detailed analysis of the impedance spectra obtained from the electrode|MIEC system. That is, one can determine all the physically important parameters of the sample under investigation directly from impedance spectroscopy, without resorting to, for example, Hall measurements to determine n or to thermogravimetry to measure K_r.

Another important property of an MIEC is the electrolytic domain boundary (EDB), which demarcates the ionically and electronically conducting regimes. From Eq. (84) the oxygen partial pressure, $p^*_{O_2}$, at which the electronic conductivity equals the ionic conductivity is defined according to

$$\sigma_{ion} = \sigma^0_{eon}\left(p^*_{O_2}\right)^{-1/4} \tag{90}$$

The smaller the $p^*_{O_2}$, the wider the electrolytic (or ionic) domain, and the more difficult it is for MIEC to be reduced. While the EDB implies a sharp distinction between ionic and electronic regimes, it is appropriate to consider the range of conditions over which the transference number ($t_{species} = \sigma_{species}/\sigma_{total}$) of the minority carrier is 0.01 or greater as the mixed conducting regime.

III. Experimental Procedure

Commercial $Sm_{0.15}Ce_{0.85}O_{1.925-\delta}$ (SDC15) powders were purchased from NexTech Materials Ltd. The loose powders were annealed at 950°C in air for 5 h in order to lower the surface area and ensure the desired sintering behavior. Pellets were uniaxially pressed at 300 MPa then sintered at 1350°C for 5 h to obtain a relative density of over 95%. The sample used for measurement was 0.78 mm thick with a diameter of 13 mm Pt ink (Engelhard 6082) was applied to both sides of the pellets (so as to cover the faces completely) and fired at 900°C for 2 h.

Two-probe AC impedance spectroscopy was performed using a Solartron 1260 impedance analyzer with a voltage amplitude of 10–40 mV and a frequency range spanning from 0.01 or 0.001 Hz to 100 K or 1M Hz. The resistance of the Pt leads was measured separately and subtracted from the raw sample data prior to analysis. The impedance was measured at 500°, 550°, 600°, and 650°C under atmospheres ranging from simulated air to 3% H_2O saturated H_2. Oxygen partial pressures from 10^{-6} to 0.21 atm were obtained from mixtures of Ar and O_2; lower oxygen partial pressures were achieved using mixtures of Ar, H_2, and H_2O, assuming a thermodynamic equilibrium between O_2, H_2, and H_2O. The gas flow rates were fixed using mass flow controllers to a total flow rate of 100 sccm, which, for the dimensions of the system utilized, implies a linear gas flow rate of ~0.74 cm/s. The whole system was allowed to stabilize under each condition before the final measurement. The typical stabilization time was 1 h under high oxygen partial pressures and 8 h under low oxygen partial pressures. In light of the small amplitude of the applied voltage and the small sample size relative to the overall flow rate and dimensions of the experimental apparatus, the gas composition is safely assumed to be unperturbed by the impedance measurement.

In order to address the challenges of directly fitting the impedance data collected under mixed conducting conditions so as to extract the five independent parameters, R_{ion}, R_{eon}, $R^{\perp}_{ion}$, $C^{\perp}_{ion}$, and C_{chem}, the analysis proceeded as follows: the ionic resistance R_{ion} and the electrode properties, $R^{\perp}_{ion}$ and $C^{\perp}_{ion}$, were first obtained from the impedance spectra in the ionic region. The electrode behavior was evaluated by fitting the data using a constant phase element (CPE) with impedance $Z_{CPE} = [(j\omega)^m Y^{\perp}]^{-1}$ rather than a pure capacitor and then determining the capacitance[2] according to $C^{\perp} = (Y^{\perp})^{1/m}(R^{\perp})^{(1/m-1)}$. As discussed above, R_{ion} is independent of p_{O_2}, and C_{ion} can be, to a first approximation, also taken to be independent of p_{O_2}. Thus, the values obtained for R_{ion}, and $C^{\perp}_{ion}$ under the ionic regime were used

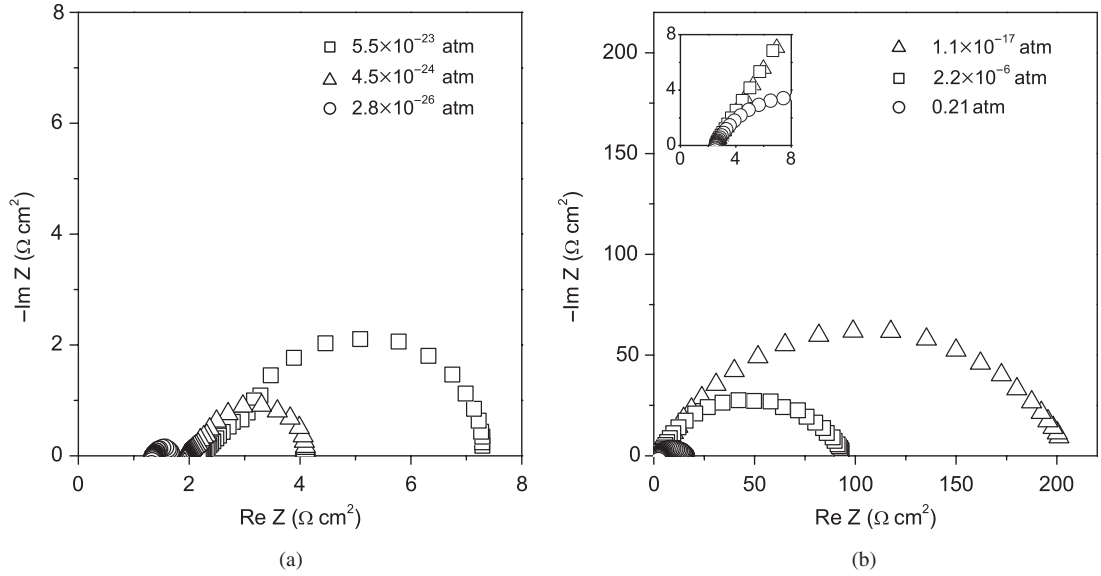

Fig. 10. Measured impedance response of Pt|SDC (samaria-doped ceria)15|Pt at 600°C under (a) reducing conditions where ceria is a mixed conductor and (b) moderately oxidizing conditions where ceria is an ionic conductor. The inset in (b) shows the high-frequency portion of the data.

as fixed parameters in the analysis of the spectra obtained under mixed conducting conditions. Those latter spectra were then fitted to Eq. (73) (i.e., simple finite-length Warburg behavior) to yield initial values for R_{eon}, $R_{\text{ion}}^{\perp}$ and $\tilde{D}$, which were further refined using a final fit to Eq. (68). It must be emphasized that such a procedure works well for a material such as ceria in which both the electrolytic and mixed conducting regimes are experimentally accessible. Alternative strategies may be required if only data from the mixed conducting regime are available.

IV. Results

Typical impedance spectra obtained from Pt|SDC15|Pt are presented in Figs. 10(a) and (b). The data were collected at 600°C at several different oxygen partial pressures. The spectra in Fig. 10(a) demonstrate that ceria is a mixed conductor at oxygen partial pressures of 5.5×10^{-23} atm and lower (at 600°C). The arcs are asymmetric, exhibiting a characteristic Warburg-like shape, and the high-frequency intercept with the real axis decreases with decreasing oxygen partial pressure. In contrast, the spectra in Fig. 10(b) reveal quite clearly that for oxygen partial pressures as low as 1.1×10^{-17} atm (at 600°C), SDC15 is a pure ionic conductor. The high-frequency intercept with the real axis is unchanged for the three measurements, and the single arc in each spectrum has the form of a depressed, yet symmetric, semi-circle.

The oxygen partial pressure dependence of the total electrical conductivity of SDC15 (as determined from the high-frequency intercept) at 500°, 550°, 600°, and 650°C is shown in Fig. 11, and the corresponding values of the ionic transference number are presented in Fig. 12. At moderate oxygen partial pressures, the conductivity is predominantly ionic and remains constant, whereas at low oxygen partial pressures, the conductivity is primarily electronic, rising as p_{O_2} decreases. The boundary between the two regions, Fig. 13, moves to higher oxygen partial pressures as the temperature increases, as expected from the temperature dependence of electronic conductivity. The position of the EDB in SDC15 is comparable with that reported for other ceria compositions.[35–37]

The experimental data of Fig. 11 are well described by Eq. (84), implied by the defect chemistry model, yielding both σ_i and σ_e^0. The Arrhenius plots for these two parameters are shown in Fig. 14. As noted above, the activation energy obtained from Fig. 14(a) for σ_i, 0.67 ± 0.01 eV, is the oxygen ion migration enthalpy, whereas that obtained from Fig. 14(b) for σ_e^0, 2.31 ± 0.02 eV, includes both the electron migration enthalpy and the reduction enthalpy.

The results presented to this point are essentially derivable from the high-frequency intercept of the types of spectra presented in Fig. 10 with the real axis. Turning to the physical parameters determined from direct fits of the impedance spectra obtained under mixed conducting conditions to $Z(\omega)$ as given in

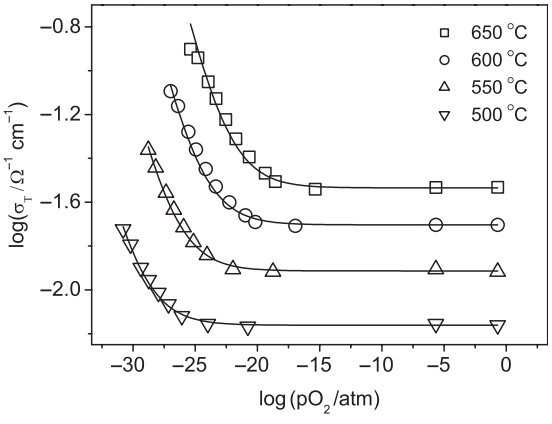

Fig. 11. Total electrical conductivity of SDC15 (samaria-doped ceria) at 500°, 550°, 600°, and 650°C as a function of oxygen partial pressure. Solid lines show the fit to $\sigma_T = \sigma_{\text{ion}} + \sigma_{\text{eon}}^0 p_{O_2}^{-1/4}$.

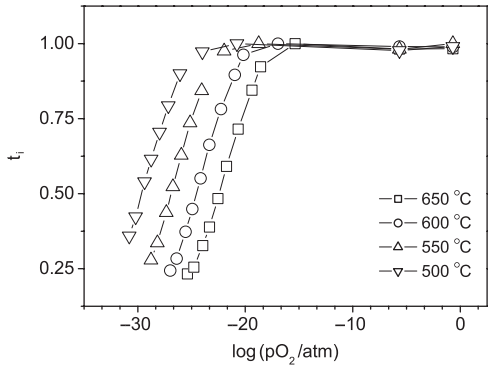

Fig. 12. Ionic transference number of SDC 15 at 500°, 550°, 600°, and 650°C as a function of oxygen partial pressure.

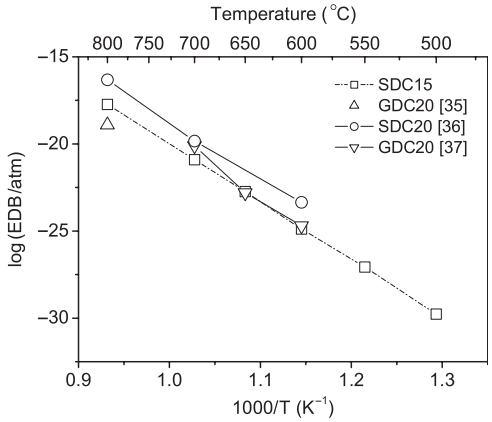

Fig. 13. Electrolytic domain boundary (EDB) as a function of temperature. Data for SDC15 (samaria-doped ceria) are the results of the present study; the points at 700° and 800°C are extrapolated values, presented to allow easy comparison with the literature data for GDC20 (gadolinia-doped ceria)[35,37] and SDC20.[36]

Eq. (68), it is important to first establish whether or not the data are well described by the Jamnik–Maier formalism. As evidenced from Fig. 15, comparisons of the measured and fitted data at 600°C and $p_{O_2} = 5.5 \times 10^{-23}$ atm, the fit to the Jamnik–Maier model is excellent. Fits to a simple Warburg expression (Eq. (73)) were acceptable under some conditions where $2R^{\perp}_{ion} \gg R_{ion} + R_{eon}$, but in most cases, the more general impedance expression given in given Eq. (68) (or Eq. (72)) was required to model the data accurately.

The MIEC properties C_{chem} and c_{eon} are shown in Figs. 16 and 17, respectively, the former in comparison with $C^{\perp}_{ion}$. As expected from Eq. (41), the behavior of C_{chem} is dominated by the concentration of electronic carriers. Furthermore, this parameter is, under all the conditions examined, far greater than $C^{\perp}_{ion}$, and $C^{\perp}_{ion}$ as measured within the electrolytic regime is indeed largely independent of p_{O_2}. Because $C_{chem} \gg C^{\perp}_{ion}$, analyses performed in which $C^{\perp}_{ion}$ was omitted from the equivalent circuit (e.g., using Eq. (72)) had a negligible impact on the quality of the fits and the values derived for the other parameters. Thus, the assumption of a constant $C^{\perp}_{ion}$ (independent of p_{O_2}), even if in error, would introduce negligible errors to the other terms.

Much as with C_{chem}, the electronic defect concentration c_{eon} also behaves as expected on the basis of the defect chemistry model. In particular, for the two lower temperature measurements, c_{eon} obeys a clear $-1/4$ power law dependence on oxygen partial pressure over the entire p_{O_2} range examined. At higher temperatures, the electronic defect concentration begins to deviate from the expected p_{O_2} dependence as the oxygen partial pressure is lowered. Under these conditions, the concentration of oxygen vacancies generated by the reduction reaction, Eq. (81), becomes significant and the oxygen vacancy concentration can no longer be treated as constant. To ensure that the approximation $\left[V_O^{\bullet\bullet}\right] = 1/2[Sm'_{Ce}]$ is adequately obeyed, further analysis is restricted to the region in which the electronic defect concentration is less than one-fifth the (extrinsic) oxygen vacancy concentration. Taking this restriction into account and fitting c_{eon} to Eq. (83), one obtains the equilibrium constant, K_r, as a function of temperature, Fig. 18. From these data, the reduction entropy ΔS_r and enthalpy ΔH_r are derived to be $1.18 \pm 0.05 \times 10^{-3}$ eV/K and 4.18 ± 0.05 eV, respectively.

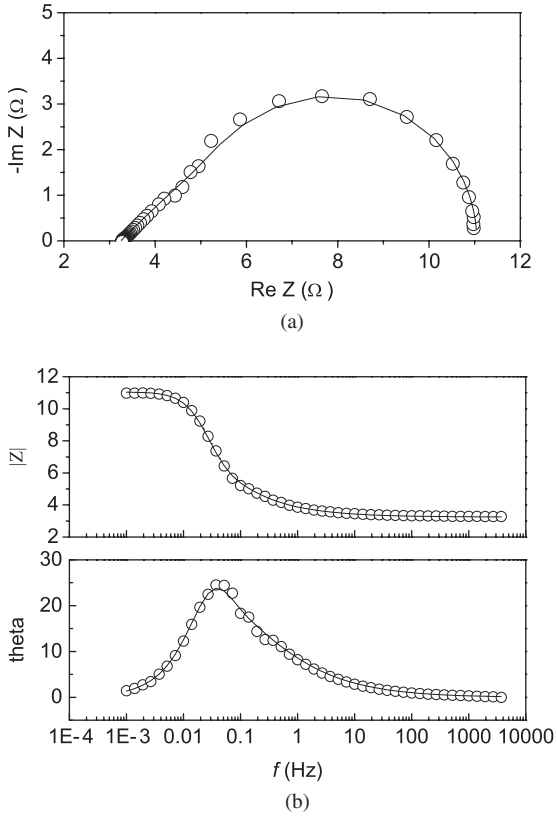

Fig. 15. Comparisons of the measured and fit impedance obtained from the Pt|SDC (samaria-doped ceria)|Pt system at 600°C and an oxygen partial pressure of 5.5×10^{-23} atm. The fit is to Eq. (68) of the main text. (a) Nyquist representation, and (b) Bode–Bode representation.

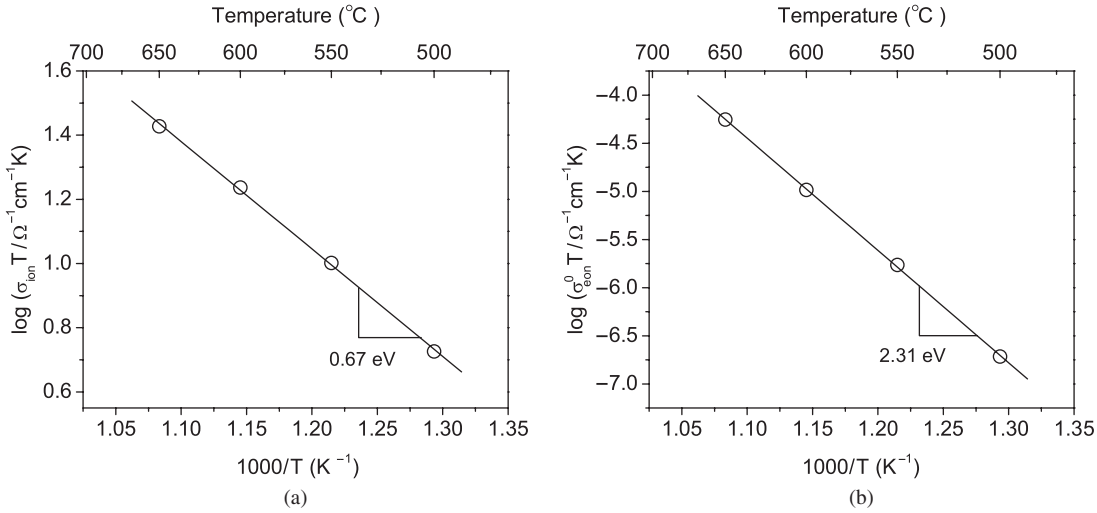

Fig. 14. (a) Ionic conductivity, σ_{ion}, and (b) oxygen partial pressure-independent term in the electronic conductivity, σ^0_{eon}, of SDC15 (samaria-doped ceria) as functions of temperature, plotted in an Arrenhius form.

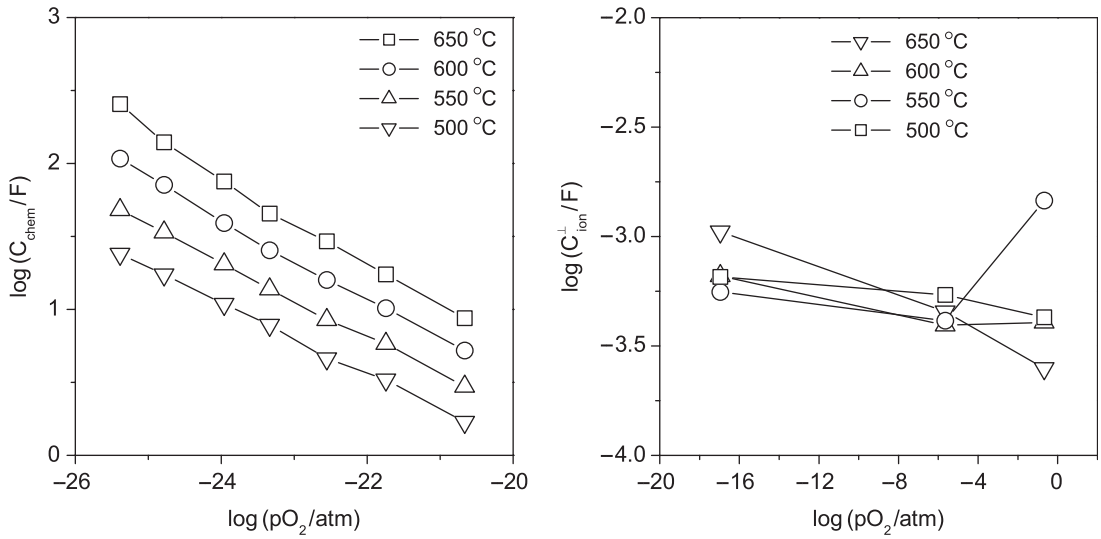

Fig. 16. (a) Chemical capacitance C_{chem}, and (b) interfacial capacitance $C_{ion}^{\perp}$ of SDC15 (samaria-doped ceria) as functions of oxygen partial pressure as determined from the measured impedance spectra with temperatures as indicated.

From the conductivities and charge carrier concentrations, Figs. 14 and 17, respectively, one can obtain both the ionic and electronic mobilities, and these are presented in Fig. 19. To allow comparison with the available literature data,[18,34] the mobilities obtained in the present work have been extrapolated to 700°C. The results clearly demonstrate that the mixed conducting behavior of doped ceria results from the very high mobility of electronic defects, which are present in much lower concentrations than the ionic defects.

Turning to the electrode behavior, the area-specific resistivity (ASR) of the Pt electrode, ρ_{Pt}, on SDC15 at 600°C is presented as a function of oxygen partial pressure in Fig. 20 in log–log form and compared with the behavior of SDC15 itself. The dashed line gives the approximate demarcation of the ionic and mixed conducting regions. In the ionic (or electrolytic) region, the electrode "conductivity" (inverse of ASR) increases with increasing oxygen partial pressure. In contrast, in the mixed conducting region, the electrode "conductivity" increases as the oxygen partial pressure is decreased. (At intermediate pressures where the electrode resistivity reached very large values, stable measurements could not be obtained.) The oxygen partial pressure dependence of $1/\rho_{Pt}$ in the two regimes is summarized in Fig. 21. Under the more oxidizing conditions of the ionic regime, the slope of log $1/\rho_{Pt}$ vs log p_{O_2} changes, even changing sign, decreasing from 0.19 at 650°C to −0.11 at 500°C. In contrast, under more reducing conditions, a −1/4 power law dependence is observed. Fitting the electrode ASR to $1/\rho_{Pt} = 1/\rho_{Pt}^{0} p_{O_2}^{-1/4}$ yields an associated activation energy for the electrode process of 2.67 ± 0.11 eV, Fig. 22. It is noteworthy that Sprague *et al.*[38] similarly observed a $p_{O_2}^{-1/4}$ dependence for the Pt electrode conductivity on mixed conducting $(Gd_{0.98}Ca_{0.02})_2 Ti_2O_7$ in CO/CO_2 atmospheres; however, a $p_{O_2}^{-1/6}$ dependence was obtained from $(Gd_{0.9}Ca_{0.1})_2 Ti_2O_7$.

Overall, the quality of the fits of the data to the Jamnik–Maier model presented here is significantly better than that reported by Atkinson *et al.*[17] in their study of Pt|$Gd_{0.1}$ $Ce_{0.9}O_{1.95-\delta}$(GDC10)|Pt. These workers investigated ceria under air and under hydrogen, with the stated objective of evaluating the validity of the Jamnik–Maier model. In addition, the sample thickness was varied so as to manipulate C_{chem} according to Eq. (41). The general observations of these authors are consistent with the results presented here. Under the electrolytic regime, the electrode arc of the Pt|GDC10|Pt system was found to be semicircular in shape, whereas it exhibited a half tear-drop shape under reducing conditions. Furthermore, the electrode resistivity derived under reducing conditions reported by Atkinson is reasonably comparable with that measured here ($\sim 30\ \Omega \cdot cm^2$ vs

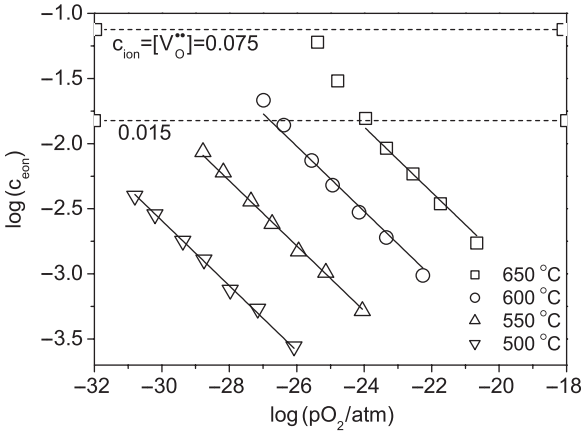

Fig. 17. Electron concentration in SDC15 (samaria-doped ceria) as a function of oxygen partial pressure as determined from the measured impedance spectra with temperatures as indicated. Solid lines indicate fits of the data to $c_{eon} = (2K_r/[Sm'_{Ce}])^{1/2} p_{O_2}^{-1/4}$. The upper dashed line corresponds to the extrinsic vacancy concentration because of acceptor doping. The lower dashed line corresponds to an electron concentration at which the approximation $2[V_O^{\bullet\bullet}] = [Sm'_{Ce}] \gg n$ is no longer valid.

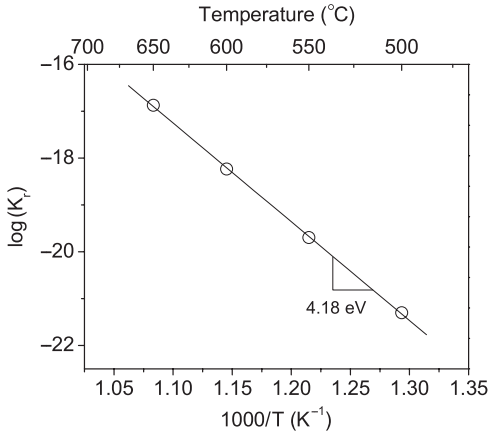

Fig. 18. Equilibrium constant for the reduction of SDC15 (samaria-doped ceria) [Eq. (81)] as a function of temperature.

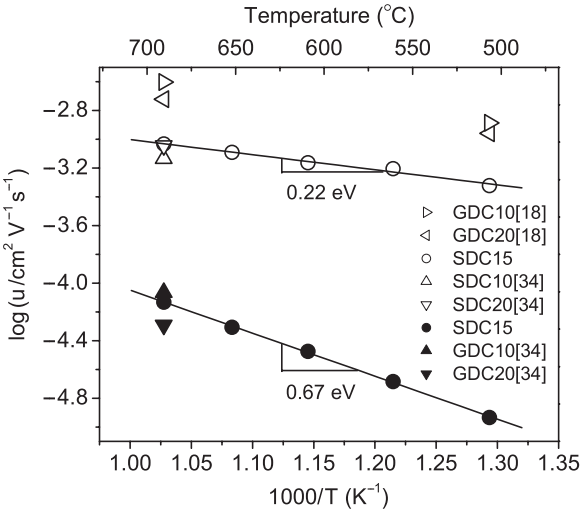

Fig. 19. Ionic and electronic mobilities as a function of temperature plotted in an Arrhenius form. Closed symbols represent for ionic mobility, whereas open symbols represent electronic mobility. The points at 700°C for SDC15 (samaria-doped ceria) represent extrapolated values, added to facilitate comparison with the literature data. Numbers in square brackets indicate the source.

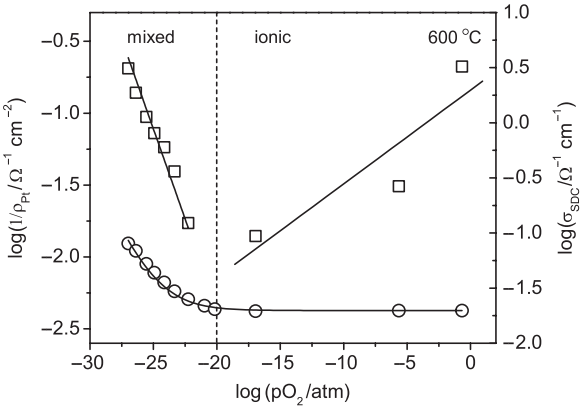

Fig. 20. Comparison of the electrolyte conductivity and inverse of the electrode area-specific resistivity in Pt|SDC (samaria-doped ceria)15|Pt at 600°C as a function of oxygen partial pressure. Solid lines show the best fits to equations given in the main text.

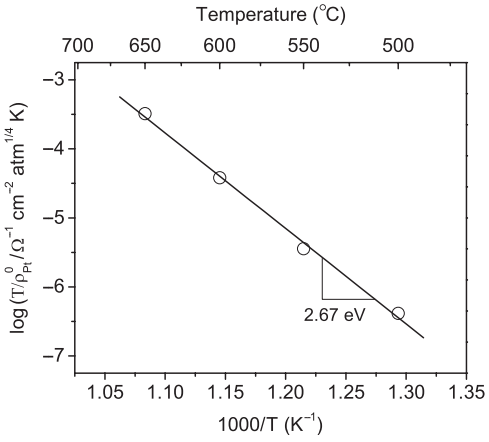

Fig. 22. Inverse of the oxygen partial pressure independent term in the electrode-specific resistivity of the Pt|SDC (samaria-doped ceria)15|Pt system as a function of temperature. Data are plotted in an Arrhenius form.

$\sim 84\ \Omega \cdot \mathrm{cm}^2$ in the present study at $T \sim 500$°C and a 10% H_2 atmosphere). The poorer quality of the fit of their data to the Jamnik–Maier model is (as pointed out by these authors) was most likely because of the fact that several materials parameters for GDC10 were taken from the literature rather than being adjusted to improve the fit, a procedure that would not have been justified given the limited dataset. Moreover, the measurements of Atkinson were performed at relatively low temperatures at which, as discussed above, complications because of grain boundary effects arise and the electrode resistance can become excessively large. While quantitative results could not be obtained because of these shortcomings, the qualitative features reported for Pt|GDC10|Pt are entirely in agreement with the observations made here on the Pt|SDC10|Pt system. Finally, it is noteworthy that Jasinski *et al.*[27] similarly obtained asymmetric low-frequency arcs from mixed conducting, undoped ceria placed between gold electrodes.

V. Discussion

(1) Properties of Ceria

The thermodynamic properties measured here for SDC15 by electrochemical methods are in good agreement with those of

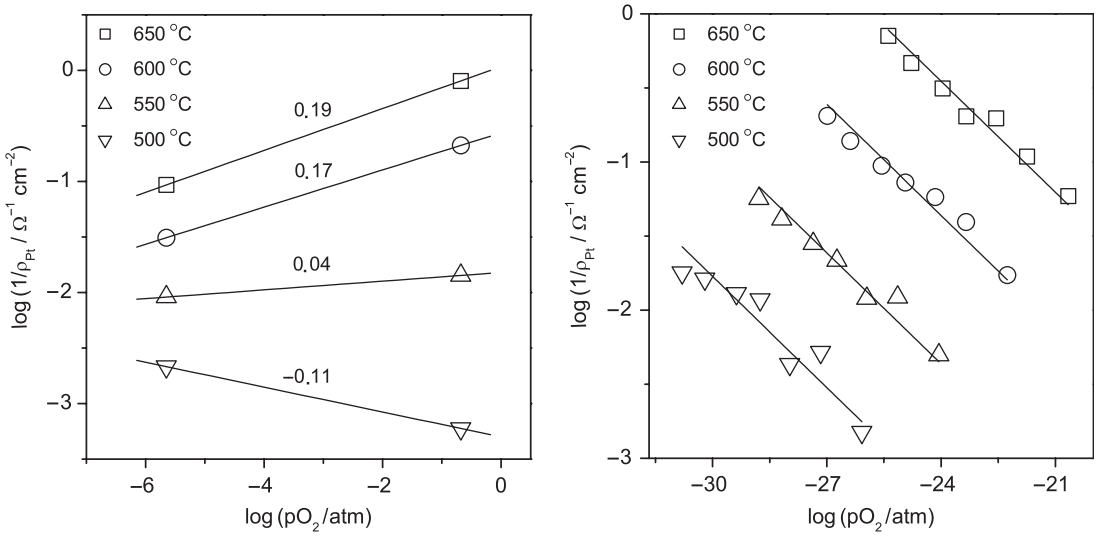

Fig. 21. Area-specific electrode resistivity of Pt|SDC (samaria-doped ceria)15|Pt as a function of oxygen partial pressure and temperature in (a) the pure ionic region, and (b) the mixed conducting region. In (a) the solid lines represent linear regression fits to the data, with the slopes as indicated. In (b), the solid lines show the fits to $1/\rho_{\mathrm{Pt}} = 1/\rho^0_{\mathrm{Pt}} p_{\mathrm{O_2}}^{-1/4}$.

Table I. Activation Energies for Ionic and Electronic Mobility, and for σ_e^0

Substance	ΔH_i (eV)	ΔH_e (eV)	ΔH_{e0} (eV)
$Ce_{0.85}Sm_{0.15}O_{1.925-\delta}$ (SDC15)	0.67 ± 0.01	0.22 ± 0.04	2.31 ± 0.02
$Ce_{0.8}Sm_{0.2}O_{1.9-\delta}$ (SDC20)[36]	0.68[†]		2.30[†]
$Ce_{0.8}Sm_{0.2}O_{1.9-\delta}$ (SDC20)[48]			2.22
$Ce_{0.9}Gd_{0.1}O_{1.95-\delta}$ (GDC10)[18]	0.64	0.25	
$Ce_{0.8}Gd_{0.2}O_{1.9-\delta}$ (GDC20)[34]	0.71	0.52	

[†]Fitted with given σ_i and σ_e^0 in Godickemeier and Gauckler.[36] SDC, Samaria-doped ceria; GDC, gadolinia-doped ceria.

related materials obtained by thermogravimetric methods. In particular, Kobayashi *et al.*[39] measured ΔS_r and ΔH_r of both $Sm_{0.1}Ce_{0.9}O_{2-\delta}$ (SDC10) and $Sm_{0.2}Ce_{0.8}O_{2-\delta}$ (SDC20). The reported enthalpies are -4.15 and -3.99 eV for SDC10 and SDC20, respectively, and the entropies -1.10×10^{-3} and -1.13×10^{-3} eV/K, respectively. If one assumes a linear dependence of reduction enthalpy and entropy on the dopant level, then one interpolates values of 4.07 eV and 1.12×10^{-3} eV/K, respectively, for the reduction enthalpy and entropy for SDC15, which are almost identical to the values of 4.18 eV and 1.18×10^{-3} eV/K, respectively, determined in this work. Given that the transport equations are derived under the assumption that the processes are not far from equilibrium, agreement between the methods is expected.

The mobilities determined here for both ions and electrons in SDC15 are also in good agreement with the literature values for related materials, Fig. 19, as are the corresponding activation energies, Table I. Specifically, the ionic mobility for SDC15 falls, in the present study, between 10^{-5} and 10^{-4} $cm^2 \cdot (V \cdot s)^{-1}$, with an activation energy of 0.67 eV. The activation energy for electron motion, 0.22 eV, is three times smaller than for ions, and the absolute mobilities are approximately one order of magnitude greater. The relatively low electronic mobility is consistent with the usual interpretation that electron motion in ceria occurs via a small polaron-activated hopping process.[40] Overall, the correspondence between the literature values of both the thermodynamic and transport properties of SDC15 and the values measured here by AC impedance spectroscopy provides strong validation of the Jamnik–Maier model for the impedance response of mixed conductors.

(2) Electrochemistry of the Pt|Ceria System

Two possible electrochemical reactions can be considered to take place on Pt under the experimental conditions used in this work. Under moderately oxidizing atmospheres (oxygen partial pressures of 10^{-6}–1 atm), the oxidation/reduction of oxygen can be described globally via the following reaction

$$\tfrac{1}{2}O_2 + 2e^- \leftrightarrow O^{2-} \tag{91}$$

Under more reducing conditions, achieved via introduction of hydrogen to the sample atmosphere, oxidation/reduction could, in principle, also occur via reaction (91), and then be followed by gas phase reaction between H_2 and O_2 to maintain an overall equilibrium between the three gaseous species (H_2, O_2, and H_2O). However, the reaction directly involving all three species is more likely,

$$H_2 + O^{2-} \leftrightarrow H_2O + 2e^- \tag{92}$$

These two sets of conditions (moderate and reducing atmospheres) and corresponding electrochemical reactions ((91) and (92), respectively) are considered separately.

The kinetics and mechanistic pathways of reaction (91) have been studied extensively in the Pt|YSZ|Pt system.[8] There is general consensus that the overall reaction rate is limited by the rate of arrival of oxygen atoms to the reaction sites at the Pt|YSZ interface. According to the model proposed by Mizusaki *et al.*,[41] at high temperatures and low oxygen partial pressures, the surface diffusion of absorbed oxygen atoms on Pt is the rate-limiting step and gives rise to a characteristic p_{O_2} dependence of the electrode resistance, obeying a $p_{O_2}^{-1/2}$ dependence at low oxygen partial pressures and a $p_{O_2}^{1/2}$ dependence at high oxygen partial pressures. Thus, the electrode "conductivity" first increases and then decreases, taking on a peak value at some intermediate pressure, $p^*_{O_2}$, which corresponds to the pressure at which the Pt coverage by oxygen atoms is 1/2. The position of the peak is temperature dependent, moving to lower p_{O_2} values as the temperature is decreased.[41,42] At low temperatures, the surface diffusion of oxygen becomes exceedingly slow, and dissociative adsorption of oxygen directly at the reaction sites become rate limiting, resulting in an electrode resistance that is independent of p_{O_2}. A transition between these two types of behavior is evident at intermediate temperatures.[41] A related model, as briefly noted in the introduction, has been proposed by Robertson and Michaels[10] and discussed further by Adler.[8] In this case, both surface diffusion and dissociative adsorption simultaneously control the overall kinetics at all temperatures, and there is no single rate-limiting step for the behavior of the electrode. An explicit p_{O_2} dependence for the electrode properties has not been derived for this model.

Because SDC15 as measured here behaves as a pure ionic conductor at moderate oxygen partial pressures, it is likely that the electrochemical reduction/oxidation of O_2 in the Pt|SDC15|Pt system occurs by a mechanism similar to that of the Pt|YSZ|Pt system. Although the limited dataset precludes definitive conclusions, the trend evident in Fig. 21(a), that of a decreasing slope with decreasing temperature, is consistent with the model described above. The data imply that $p^*_{O_2}$ is greater than 1 atm at 650°C and less than 10^{-6} atm at 500°C, not unreasonable values in comparison with those reported for YSZ.[43] In addition, the SDC system examined here is similar to YSZ[42,44] in that both show only one electrode-related arc with a symmetric, semi-circular appearance in their respective impedance spectra, further supporting the conclusion that the mechanisms must be similar. It is possible that upon treatment of the raw impedance data as described by Adler[8] for porous Pt electrodes on single-crystal zirconia, an underlying finite-length Warburg or Gerischer type of response would be obtained, consistent with the proposal that diffusion/adsorption limits the electrochemical reduction of oxygen. That the absolute magnitude of the area-specific electrode resistance measured here, approximately $5\,\Omega \cdot cm^2$ at 600°C, is much lower than that reported for Pt|YSZ,[42,44] approximately $500\,\Omega \cdot cm^2$, is likely because of differences in Pt microstructure that influence the diffusion length and the density of the reaction sites.

Alternatively, one cannot rule out the possibility that the charge transfer reaction, in which adsorbed oxygen atoms on the Pt surface react with electrons and form oxygen ions on the electrolyte surface, is the rate-limiting step. Such a mechanism was proposed much earlier from the study of the polarization phenomenon on Pt|ceria, in particular, by Wang and Nowick.[45,46] In this case, a slope of $-1/4$ is expected at a low oxygen partial pressure in a log–log plot of $1/\rho$ vs p_{O_2}, which gradually shifts to a value of $+1/4$ at a high oxygen partial pressure. As pointed out by Mizusaki *et al.*,[41] the data presented by Wang and Nowick have not been collected over a sufficiently wide oxygen partial pressure range to distinguish between slopes

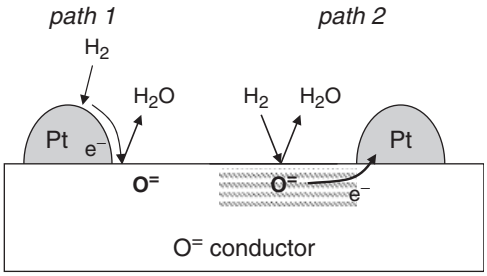

Fig. 23. Schematic diagram showing the hydrogen electro-oxidation pathways (left) on Pt|YSZ (yttria-stabilized zirconia) and (right) Pt|SDC (samaria-doped ceria).

of $\pm 1/2$ from those of $\pm 1/4$ and conclusively support the charge transfer model. Thus, we propose that diffusion/dissociative adsorptions of oxygen are the rate-limiting steps in the Pt|SDC15|Pt system under oxygen atmospheres, much as is widely accepted for Pt|YSZ|Pt.

In comparison with the behavior of O_2 on Pt, the electrochemistry of the H_2–H_2O system is quite complex because many more active species can be involved in the electrochemical oxidation/reduction steps. As a consequence, no real consensus as to the reaction pathway has emerged in the literature, even for Pt|YSZ|Pt. While Mizusaki *et al.*,[47] who observed only one electrode-related arc in their impedance spectra, have suggested that OH group transfer across the Pt|YSZ is rate limiting, several other groups have argued that multiple, serial steps are necessary to describe the reaction on the basis of the observation of multiple (2–3) electrode-related responses by impedance spectroscopy. In particular, a high-frequency arc has been attributed to the charge transfer step and a low-frequency arc to hydrogen dissociative adsorption on the Pt surface.[25] As noted above, it is not possible to detect by impedance spectroscopy serial reaction steps at the electrode–sample interface for a sample that is a mixed ionic and electronic conductor with a large value of C_{chem}. Thus, it is not possible to establish directly whether Pt|SDC15|Pt exhibits a single or a multistep step mechanism. Nevertheless, from the p_{O_2}-dependent behavior of ρ_{Pt} measured here, Fig. 21(b), we can immediately conclude that electro-oxidation of hydrogen on Pt|ceria occurs by a fundamentally different mechanism than it does on Pt|zirconia. Indeed, in the case of Pt|YSZ, there is no reason to expect a direct dependence of ρ_{Pt} on p_{O_2} in the presence of H_2. Instead, because adsorbed hydrogen atoms and hydroxyl groups are presumed to participate in the reaction mechanism, dependencies on p_{H_2} or p_{H_2O} are typically probed (which only depend indirectly on p_{O_2} via the gas-phase equilibrium).

The observation of a power law of $p_{O_2}^{-1/4}$ here suggests that the electrode reactions are correlated to the electronic conductivity of mixed conducting ceria, which exhibits precisely the same dependence on oxygen partial pressure. Furthermore, the activation energy of $1/\rho_{Pt}^0$, 2.67 ± 0.11 eV, is almost identical to that measured for the electronic conductivity of SDC15, 2.31 ± 0.02 eV. Based on these observations, we propose that the electrochemical reaction 92 can occur via two parallel paths on oxygen ion-conducting materials (Fig. 23). In the first path, dissociative hydrogen desorption occurs on the Pt surface, followed by migration of protons to the Pt|oxide interface and subsequent electrochemical reaction. In the second path, hydrogen desorption occurs directly on the oxide surface, which subsequently reacts electrochemically with oxygen, yielding up electrons that are then transported through the oxide to the Pt. Given the very low electronic conductivity of zirconia, the second pathway is not available for this electrolyte and the reaction is taken to occur via the first path, with the exact rate-limiting step yet to be determined. In the case of ceria, we propose that although the first path is probably fast, the second path is faster. That is, we propose that the electrochemical reaction occurs directly on the ceria surface (i.e., that ceria is electrochemically active), and that the reaction is limited by the rate of removal of electrons from the reaction sites (i.e., electronic conductivity).

VI. Summary and Conclusions

A rigorous derivation of the AC impedance of mixed conducting materials has been presented. Using $Pt|Sm_{0.15}Ce_{0.85}O_{1.925-\delta}|Pt$ as a model system, it is demonstrated that the impedance data yield a broad range of electrical and electrochemical properties of the mixed conductors. In particular, the concentration of free electron carriers, the mobilities and activation energies for both ion and electron transport, the EDB, and the entropy and enthalpy of electrochemical reduction have all been measured. The values are in good agreement with what would be expected based on the reported properties of Sm- and Gd-doped ceria with differing compositions. The results not only validate the model originally proposed by Jamnik and Maier but also demonstrate and exploit its full capabilities.

The oxygen reduction reaction on $Pt|Sm_{0.15}Ce_{0.85}O_{1.925-\delta}$ has not been extensively studied here, but the data nevertheless suggest that a mechanism similar to that on Pt|YSZ is operative. Specifically, the data are consistent with a model in which oxygen surface diffusion to reaction sites is rate limiting. The hydrogen oxidation reaction, in contrast, occurs by a mechanism quite distinct from that on YSZ. Here, the electrode "conductivity" is found to obey a $-1/4$ power law dependence on oxygen partial pressure, $1/\rho_{Pt} = 1/\rho_{Pt}^0 p_{O_2}^{-1/4}$, with an activation energy for $1/\rho_{Pt}^0$ that is almost identical to that measured for the electronic conductivity. Accordingly, it is postulated that ceria is electrochemically active for hydrogen oxidation, with the reaction occurring directly on the ceria surface and limited by the rate of removal of electrons from the reaction sites.

The geometric features of the impedance spectra measured here for SDC15 are in accord with the model put forth by Jamnik and Maier. In the electrolytic regime, simple arcs are obtained in the complex plane, whereas under conditions where ceria behaves as a mixed conductor, the spectra are asymmetric, half tear-drop shaped. The large value of the chemical capacitance under mixed conducting conditions overwhelms the electrode capacitance and obscures any fine detail in the impedance spectra resulting from a possible multi-step process at the electrodes. This is precisely the oxygen partial pressure regime relevant for probing the hydrogen electro-oxidation process. Despite this limitation of the experimental data, the oxygen partial pressure dependence of the electrode resistance on oxygen partial pressure provides strong evidence for the electrochemical activity of ceria.

Appendix

The impedance of the general electrode|MIEC|electrode system represented in Fig. 5 (omitting the dielectric capacitance term, C_{dielc}) of the main text can be evaluated by first recasting the circuit from one comprised of R and C to one comprised of elements with arbitrary impedance in Fig. A1.

Here, Z_A and Z_B are the terminal impedances corresponding to the impedance of the electrode|MIEC to ion and electron transfer, respectively. Z_1 and Z_2 are the unit impedances in rails 1 and 2, respectively, whereas Z_3 is the impedance between rails 1 and 2. V_a and V_b are the input and output voltages, respec-

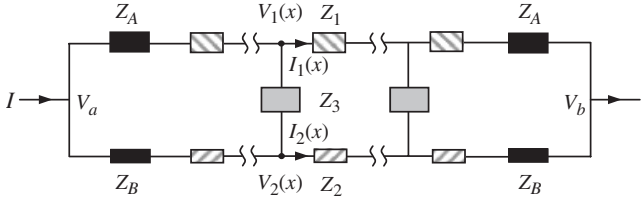

Fig. A1. Generalized circuit.

tively. I is the total current. $V_1(x)$ and $I_1(x)$ are the voltage and current for the branch point in rail 1. $V_2(x)$ and $I_2(x)$ are the voltage and current for the branch point in rail 2. A circuit having this topology is often referred to as a transmission line model or a ladder network.

$$Z_1 = Z_1^{\text{Total}} \frac{\mathrm{d}x}{L} \tag{A-1}$$

$$Z_2 = Z_2^{\text{Total}} \frac{\mathrm{d}x}{L} \tag{A-2}$$

$$Z_3 = Z_3^{\text{Total}} \frac{L}{\mathrm{d}x} \tag{A-3}$$

Ohm's law implies

$$\frac{\mathrm{d}V_1(x)}{\mathrm{d}x} = -\frac{Z_1^{\text{Total}}}{L} I_1(x) \tag{A-4}$$

$$\frac{\mathrm{d}V_2(x)}{\mathrm{d}x} = -\frac{Z_2^{\text{Total}}}{L} I_2(x) \tag{A-5}$$

Kirchoff's law implies

$$-\frac{\mathrm{d}I_1(x)}{\mathrm{d}x} = \frac{\mathrm{d}I_2(x)}{\mathrm{d}x} = \frac{V_1(x) - V_2(x)}{Z_3^{\text{Total}} L} \tag{A-6}$$

$$I = I_1(x) + I_2(x) \tag{A-7}$$

And the boundary conditions are:

$$V_a - V_1(0) = Z_A I_1(0) \tag{A-8}$$

$$V_a - V_2(0) = Z_B I_2(0) \tag{A-9}$$

$$V_1(L) - V_b = Z_A I_1(L) \tag{A-10}$$

$$V_2(L) - V_b = Z_B I_2(L) \tag{A-11}$$

$$V_a - V_b = ZI \tag{A-12}$$

where Z is the total impedance. From Eqs. (A-4)–(A-7), one obtains

$$Z_3^{\text{Total}} L^2 I_1'' - \left(Z_1^{\text{Total}} + Z_2^{\text{Total}}\right) I_1 + Z_2^{\text{Total}} I = 0 \tag{A-13}$$

The solution to Eq. (A-13) is

$$I_1(x) = \frac{Z_2^{\text{Total}}}{Z_1^{\text{Total}} + Z_2^{\text{Total}}} I + C_1 \mathrm{e}^{kx} + C_2 \mathrm{e}^{-kx} \tag{A-14}$$

with

$$k = \frac{1}{L}\sqrt{\frac{Z_1^{\text{Total}} + Z_2^{\text{Total}}}{Z_3^{\text{Total}}}} \tag{A-15}$$

The solutions to other parameters are

$$I_2(x) = \frac{Z_1^{\text{Total}}}{Z_1^{\text{Total}} + Z_2^{\text{Total}}} I - C_1 \mathrm{e}^{kx} - C_2 \mathrm{e}^{-kx} \tag{A-16}$$

$$V_1(x) = -\frac{Z_1^{\text{Total}} Z_2^{\text{Total}}}{Z_1^{\text{Total}} + Z_2^{\text{Total}}} \frac{x}{L} I - \frac{C_1 Z_1^{\text{Total}}}{kL} \mathrm{e}^{kx} + \frac{C_2 Z_1^{\text{Total}}}{kL} \mathrm{e}^{-kx} \tag{A-17}$$

$$V_2(x) = -\frac{Z_1^{\text{Total}} Z_2^{\text{Total}}}{Z_1^{\text{Total}} + Z_2^{\text{Total}}} \frac{x}{L} I + \frac{C_1 Z_2^{\text{Total}}}{kL} \mathrm{e}^{kx} - \frac{C_2 Z_2^{\text{Total}}}{kL} \mathrm{e}^{-kx} \tag{A-18}$$

Applying boundary conditions, Eqs. (A-8)–(A-12), one obtains

$$Z = \frac{Z_1^{\text{Total}} Z_2^{\text{Total}}}{Z_1^{\text{Total}} + Z_2^{\text{Total}}} + \frac{2}{Z_1^{\text{Total}} + Z_2^{\text{Total}}} \cdot \frac{kLZ_AZ_B(Z_1^{\text{Total}} + Z_2^{\text{Total}}) + \left[(Z_2^{\text{Total}})^2 Z_A + (Z_1^{\text{Total}})^2 Z_B\right] \tanh\left(\frac{kL}{2}\right)}{kL(Z_A + Z_B) + (Z_1^{\text{Total}} + Z_2^{\text{Total}}) \tanh\left(\frac{kL}{2}\right)} \tag{A-19}$$

By definition, for the circuit in Fig. 5, one obtains

$$Z_1^{\text{Total}} = R_{\text{ion}} \tag{A-20}$$

$$Z_2^{\text{Total}} = R_{\text{eon}} \tag{A-21}$$

$$Z_3^{\text{Total}} = 1/(\mathrm{j}\omega C_{\text{chem}}) \tag{A-22}$$

$$Z_A = Z_{\text{ion}}^{\perp} \tag{A-23}$$

$$Z_B = Z_{\text{eon}}^{\perp} \tag{A-24}$$

Using these and the definition

$$\tilde{D} = \frac{L^2}{(R_{\text{ion}} + R_{\text{eon}}) C_{\text{chem}}} \tag{A-25}$$

the argument of the tanh can be evaluated as follows:

$$k = \sqrt{\frac{(R_{\text{ion}} + R_{\text{eon}})\mathrm{j}\omega C_{\text{chem}}}{L^2}} = \sqrt{\frac{\mathrm{j}\omega}{\tilde{D}}} \Rightarrow \frac{kL}{2} = \sqrt{\frac{\mathrm{j}\omega L^2}{4\tilde{D}}} \tag{A-26}$$

simple algebraic manipulation then yields

$$Z(\omega) = Z_\infty + (Z_0 - Z_\infty) \times \frac{\tanh\sqrt{\frac{\mathrm{j}\omega L^2}{4\tilde{D}}} + \frac{R_{\text{ion}} + R_{\text{eon}}}{2\left(Z_{\text{ion}}^{\perp} + Z_{\text{eon}}^{\perp}\right)} \tanh\sqrt{\frac{\mathrm{j}\omega L^2}{4\tilde{D}}}}{\sqrt{\frac{\mathrm{j}\omega L^2}{4\tilde{D}}} + \frac{R_{\text{ion}} + R_{\text{eon}}}{2\left(Z_{\text{ion}}^{\perp} + Z_{\text{eon}}^{\perp}\right)} \tanh\sqrt{\frac{\mathrm{j}\omega L^2}{4\tilde{D}}}} \tag{A-27}$$

with

$$\frac{1}{Z_0} = \frac{1}{R_{\text{ion}} + 2Z_{\text{ion}}^{\perp}} + \frac{1}{R_{\text{eon}} + 2Z_{\text{eon}}^{\perp}} \tag{A-28}$$

and

$$Z_\infty = \frac{R_{\text{ion}} R_{\text{eon}}}{R_{\text{ion}} + R_{\text{eon}}} + 2\frac{Z_{\text{ion}}^{\perp} Z_{\text{eon}}^{\perp}}{Z_{\text{ion}}^{\perp} + Z_{\text{eon}}^{\perp}} \tag{A-29}$$

Eq. (A-27) differs from Eq. (7) given in Jamnik and Maier[13] by the term $(Z_0 - Z_\infty)$, which has apparently been omitted from that paper because of a typographical misprint.

Acknowledgments

We are grateful to Derek Johnson at Scribner Associates for modifying the software package *ZView* to enable the analyses reported here.

References

[1]S. P. Jiang, J. G. Love, and S. P. S. Badwal, "Electrochemical Techniques in Studies of Solid Ionic Conductors," *Key Eng. Mater.*, **125–126**, 81–132 (1997).

[2]J. R. MacDonald and W. B. Johnson, "Fundamentals of Impedance Spectroscopy," pp. 1–26 in *Impedance Spectroscopy: Emphasizing Solid Materials*

and Systems, Edited by J. R. MacDonald. John Wiley and Sons, New York, 1987.
[3]ISI Web of Knowledge, Thomson Scientific, 04/30/05.
[4]E. Warburg, "Uber das Verhalten Sogenannter Unpolarisirbarer Elektroden Gegen Wechselstrom," *Ann. Phys. Chem.*, **67** [3] 493–9 (1899).
[5]E. Warburg, "Uber die Polarizationscapacität des Plations," *Ann. Phys.*, **6**, 125–35 (1901).
[6]B. A. Boukamp, "Electrochemical Impedance Spectroscopy in Solid State Ionics: Recent Advances," *Solid State Ionics*, **169** [1–4] 65–73 (2004).
[7]B. A. Boukamp and H. J. M. Bouwmeester, "Interpretation of the Gerischer Impedance in Solid State Ionics," *Solid State Ionics*, **157** [1–4] 29–33 (2003).
[8]S. B. Adler, "Factors Governing Oxygen Reduction in Solid Oxide Fuel Cell Cathodes," *Chem. Rev.*, **104** [10] 4791–43 (2004).
[9]M. Sluyters-Rehbach and J. H. Sluyters, "A.C. Techniques," p. 274 in *Comprehensive Treatise of Electrochemistry*, Vol. 9, Edited by E. Yeager, J. O'M. Bockris, B. E. Conway, and S. Sarangapani. Plenum, New York, 1984.
[10]N. L. Robertson and J. N. Michaels, "Oxygen-Exchange on Platinum-Electrodes in Zirconia Cells—Location of Electrochemical Reaction Sites," *J. Electrochem. Soc.*, **137** [1] 129–35 (1990).
[11]H. Gerischer, "Wechselstrompolarisation von Elektroden mit einem Potentialbestimmenden Schritt beim Gleichgewichtspotential I," *Z. Phys. Chem.*, **198**, 286–313 (1951).
[12]J. Jamnik and J. Maier, "Generalised Equivalent Circuits for Mass and Charge Transport: Chemical Capacitance and its Implications," *Phys. Chem. Chem. Phys.*, **3** [9] 1668–78 (2001).
[13]J. Jamnik and J. Maier, "Treatment of the Impedance of Mixed Conductors—Equivalent Circuit Model and Explicit Approximate Solutions," *J. Electrochem. Soc.*, **146** [11] 4183–8 (1999).
[14]A. A. Moya, A. Hayas, and J. Horno, "Steady-State, Transient and Small-Amplitude AC Responses of an Electrochemical Cell with Immobile Background Charge: A Network Approach," *Solid State Ionics*, **130** [1–2] 9–17 (2000).
[15]J. R. Macdonald, "Theory of Space-Charge Polarization and Electrode-Discharge Effects," *J. Chem. Phys.*, **58** [11] 4982–5001 (1973).
[16]T. R. Brumleve and R. P. Buck, "Transmission-Line Equivalent-Circuit Models for Electrochemical Impedances," *J. Electroanal. Chem.*, **126** [1–3] 73–104 (1981).
[17]A. Atkinson, S. A. Baron, and N. P. Brandon, "AC Impedance Spectra Arising from Mixed Ionic Electronic Solid Electrolytes," *J. Electrochem. Soc.*, **151** [5] E186–93 (2004).
[18]B. C. H. Steele, "Appraisal of $Ce_{1-y}Gd_yO_{2-y/2}$ Electrolytes for IT-SOFC Operation at 500°C," *Solid State Ionics*, **129** [1–4] 95–110 (2000).
[19]Z. P. Shao and S. M. Haile, "A High-Performance Cathode for the Next Generation of Solid-Oxide Fuel Cells," *Nature*, **431** [7005] 170–3 (2004).
[20]M. Mogensen, N. M. Sammes, and G. A. Tompsett, "Physical, Chemical and Electrochemical Properties of Pure and Doped Ceria," *Solid State Ionics*, **129** [1–4] 63–94 (2000).
[21]H. Richert, *Electrochemistry of Solids* pp. 79–87. Springer-Verlag, Berlin, 1982.
[22]A. D. Pelton, "The Chemical Capacitance—A Thermodynamic Solution Property," *J. Chim. Phys.*, **89** [10] 1931–49 (1992).
[23]H. C. Chang and G. Jaff, "Polarization in Electrolytic Solutions. 1. Theory," *J. Chem. Phys.*, **20** [7] 1071–107 (1952).
[24]D. R. Franceschetti, J. R. Macdonald, and R. P. Buck, "Interpretation of Finite-Length-Warburg-Type Impedances in Supported and Unsupported Electrochemical-Cells with Kinetically Reversible Electrodes," *J. Electrochem. Soc.*, **138** [5] 1368–71 (1991).
[25]S. P. Jiang and S. P. S. Badwal, "Hydrogen Oxidation at the Nickel and Platinum Electrodes on Yttria-Tetragonal Zirconia Electrolyte," *J. Electrochem. Soc.*, **144** [11] 3777–84 (1997).
[26]X. Guo, W. Sigle, and J. Maier, "Blocking Grain Boundaries in Yttria-Doped and Undoped Ceria Ceramics of High Purity," *J. Am. Ceram. Soc.*, **86** [1] 77–87 (2003).
[27]P. Jasinski, V. Petrovsky, T. Suzuki, and H. U. Anderson, "Impedance Studies of Diffusion Phenomena and Ionic and Electronic Conductivity of Cerium Oxide," *J. Electrochem. Soc.*, **152** [4] J27–32 (2005).
[28]S. Kim and J. Maier, "On the Conductivity Mechanism of Nanocrystalline Ceria," *J. Electrochem. Soc.*, **149** [10] J73–83 (2002).
[29]A. Tschope, "Interface Defect Chemistry and Effective Conductivity in Polycrystalline Cerium Oxide," *J. Electroceram.*, **14** [1] 5–23 (2005).
[30]J. Jamnik, "Impedance Spectroscopy of Mixed Conductors with Semi-Blocking Boundaries," *Solid State Ionics*, **157** [1–4] 19–28 (2003).
[31]J. Bisquert, "Theory of the Impedance of Electron Diffusion and Recombination in a Thin Layer," *J. Phys. Chem.*, **106** [2] 325–33 (2002).
[32]N. Q. Minh and T. Takahashi, "Electrical Conduction in Ceramics," pp. 41–69 in *Science and Technology of Ceramic Fuel Cells*. Elsevier Science, Amsterdam, 1995.
[33]Y. M. Chiang, D. P. Birnie III, and W. D. Kingery, "Defects in Ceramics, " pp. 101–81 in *Physical Ceramics: Principles for Ceramics Science and Engineering*. John Wiley & Sons, New York, 1997.
[34]S. R. Wang, T. Kobayashi, M. Dokiya, and T. Hashimoto, "Electrical and Ionic Conductivity of Gd-Doped Ceria," *J. Electrochem. Soc.*, **147** [10] 3606–9 (2000).
[35]H. L. Tuller and A. S. Nowick, "Doped Ceria as a Solid Oxide Electrolyte," *J. Electrochem. Soc.*, **122** [2] 255–9 (1975).
[36]M. Godickemeier and L. J. Gauckler, "Engineering of Solid Oxide Fuel Cells with Ceria-Based Electrolytes," *J. Electrochem. Soc.*, **145** [2] 414–21 (1998).
[37]S. Lubke and H. D. Wiemhofer, "Electronic Conductivity of Gd-Doped Ceria with Additional Pr-Doping," *Solid State Ionics*, **117** [3–4] 229–43 (1999).
[38]J. J. Sprague, O. Porat, and H. L. Tuller, "Mixed Conducting Gas Sensors: Atmosphere Dependent Electrode Impedance," *Sens. Actuators B*, **36** [1–3] 348–52 (1996).
[39]T. Kobayashi, S. R. Wang, M. Dokiya, H. Tagawa, and T. Hashimoto, "Oxygen Nonstoichiometry of $Ce_{1-y}Sm_yO_{2-0.5y-x}$ ($y = 0.1, 0.2$)," *Solid State Ionics*, **126** [3–4] 349–57 (1999).
[40]H. L. Tuller, "Mixed Conduction in Nonstoichiometric Oxides," pp. 310–5 in *Nonstoichiometric Oxides*, Edited by O. T. Sorensen. Academic Press, New York, 1981.
[41]J. Mizusaki, K. Amano, S. Yamauchi, and K. Fueki, "Electrode-Reaction at $Pt,O_2(g)$/Stabilized Zirconia Interfaces. 1. Theoretical Consideration of Reaction Model," *Solid State Ionics*, **22** [4] 313–22 (1987).
[42]J. Vanherle and A. J. McEvoy, "Impedance Characteristics of Platinum-Electrodes on Yttria-Stabilized Zirconia," *Ber. Bunsen. Phys. Chem.*, **97** [3] 470–4 (1993).
[43]J. Mizusaki, K. Amano, S. Yamauchi, and K. Fueki, "Electrode-Reaction at Pt,O_2 (g)/Stabilized Zirconia Interfaces. 2. Electrochemical Measurements and Analysis," *Solid State Ionics*, **22** [4] 323–30 (1987).
[44]W. F. Zhang, P. Schmidt-Zhang, and U. Guth, "Electrochemical Studies on Cells M/YSZ/Pt (M = Pt, Pt-Ga_2O_3) in NO, O_2, N_2 Gas Mixtures," *Solid State Ionics*, **169** [1–4] 121–8 (2004).
[45]D. Y. Wang and A. S. Nowick, "Cathodic and Anodic Polarization Phenomena at Platinum-Electrodes with Doped CeO_2 as Electrolyte. 1. Steady-State Overpotential," *J. Electrochem. Soc.*, **126** [7] 1155–65 (1979).
[46]D. Y. Wang and A. S. Nowick, "Cathodic and Anodic Polarization Phenomena at Platinum-Electrodes with Doped CeO_2 as Electrolyte. 2. Transient Overpotential and AC Impedance," *J. Electrochem. Soc.*, **126** [7] 1166–72 (1979).
[47]J. Mizusaki, H. Tagawa, K. Isobe, M. Tajika, I. Koshiro, H. Maruyama, and K. Hirano, "Kinetics of the Electrode-Reaction at the H_2–H_2O Porous Pt Stabilized Zirconia Interface," *J. Electrochem. Soc.*, **141** [6] 1674–83 (1994).
[48]Y. P. Xiong, K. Yamaji, T. Horita, N. Sakai, and H. Yokokawa, "Hole and Electron Conductivities of 20 mol%-$ReO_{1.5}$ Doped CeO_2 (Re = Yb, Y, Gd, Sm, Nd, La)," *J. Electrochem. Soc.*, **151** [3] A407–12 (2004). □

Sossina M. Haile is Associate Professor of Materials Science and of Chemical Engineering at the California Institute of Technology. She earned her Ph.D. in Materials Science and Engineering from the Massachusetts Institute of Technology in 1992. As part of her doctoral studies, Haile spent a year as a Fulbright Fellow at the Max Plank Institute for Solid State Research, Stuttgart, Germany. She then held a postdoctoral appointment at this same institution as a Humboldt Fellow. Before assuming her present position at Caltech in 1996, Haile was a member of the faculty at the University of Washington. Her research broadly encompasses solid state ionic materials and devices, with particular focus on fuel cells. She has established a new class of fuel cells based on solid acid electrolytes, and demonstrated record power densities for solid oxide fuel cells. Haile has published over 60 papers on these topics and has been an invited speaker at several national and international conferences. In 1992 she was awarded a National Young Investigator Award from the National Science Foundation. Her other major awards include the 1997 Robert L. Hardy Award of the Minerals, Metals and Materials Society (TMS), the 2000 Robert L. Coble Award of the American Ceramic Society and the 2001 J. Bruce Wagner Jr. Young Investigator Award of the Electrochemical Society. Haile has served as a principal editor for the Journal of Materials Research (1997–2001), and is presently a member of the National Materials Advisory Board of the National Academies of Sciences and Engineering.

Wei Lai is a graduate student in Materials Science at the California Institute of Technology. He received his B.S. (1998) and M.S. (2001) in Materials Science and Engineering from the University of Science and Technology of China, China. His research work focuses on the electrochemistry and microstructure of materials for intermediate temperature solid oxide fuel cells. His recent awards include the 2005 Graduate Excellence in Materials Science Diamond Award of the Basic Science Division of the American Ceramic Society and the 2005 Li Ming Scholarship of the California Institute of Technology.